THE JOURNAL OF PHYSICAL CHEMISTRY A

pubs.acs.org/JPCA Article

Visible, Near-Infrared, and Dual-Range Luminescence Spanning the 4f Series Sensitized by a Gallium(III)/Lanthanide(III) Metallacrown Structure

Elvin V. Salerno,[‡] Svetlana V. Eliseeva,*[,‡] Bernadette L. Schneider, Jeff W. Kampf, Stéphane Petoud,* and Vincent L. Pecoraro*

Cite This: *J. Phys. Chem. A* 2020, 124, 10550−10564 Read Online

ACCESS | Metrics & More | Article Recommendations | Supporting Information

ABSTRACT: Lanthanide(III) ions (Ln^{3+}) in coordination compounds exhibit unique luminescence properties with narrow and characteristic f-f transitions throughout the visible and near-infrared (NIR) ranges. In addition, some Ln^{3+} such as Pr^{3+}, Sm^{3+}, Dy^{3+}, Ho^{3+}, Er^{3+}, and Tm^{3+} possess an exceptional ability, although less explored, to exhibit dual-range emissions. Such remarkable features allow highly specific use in materials science and biology, for example, for the creation of sophisticated barcode modules or for the next generation of optical imaging applications. Herein, a series of Ga^{3+}/Ln^{3+} metallacrowns (MCs) with the general composition $[LnGa_8(shi)_8(OH)_4]Na{\cdot}xCH_3OH{\cdot}yH_2O$ (**Ln-1**, Ln = Pr^{3+}, Nd^{3+}, Sm^{3+}−Yb^{3+} and analogue Y^{3+}; H_3shi = salicylhydroxamic acid) is presented. **Ln-1** were obtained by reacting Ga^{3+} and Ln^{3+} nitrate salts with the H_3shi ligand. X-ray single crystal unit cell analysis confirmed that all MCs are isostructural. The crystal structure was solved for the Nd^{3+} analogue and revealed that Nd^{3+} is centered between two [12-$MC_{Ga^{III}N(shi)}$-4] MC rings and bound to eight hydroximate oxygen ions (four from each ring) in a pseudosquare antiprismatic fashion adopting a pseudo-D_{4h} symmetry. Pulsed gradient spin echo diffusion ordered ^{1}H NMR spectroscopy and electrospray ionization mass spectrometry confirmed that the structure of **Ln-1** remains intact in methanol solutions while mass spectrometry suggests that four OH^- bridges are exchanged with CH_3O^-/CD_3O^-. An exceptional ability of this series of MCs to sensitize the characteristic emission of Ln^{3+} was confirmed with the observation of bright red and green emission signals of **Eu-1** and **Tb-1**, NIR emissions of **Yb-1** and **Nd-1**, and dual-range emissions of **Pr-1**, **Sm-1**, **Dy-1**, **Ho-1**, **Er-1**, and **Tm-1** in the solid state upon excitation into ligand-centered bands at 340 nm. The luminescence properties of **Ln-1** (Ln = Nd^{3+}, Sm^{3+}, Eu^{3+}, Tb^{3+}, Dy^{3+}, and Yb^{3+}) were also investigated in CH_3OH and CD_3OD solutions. For **Eu-1** and **Yb-1** MCs, more extensive analyses of the photophysical properties were performed, which included the determination of radiative lifetimes, intrinsic quantum yields, and sensitization efficiencies. The absolute quantum yields (Q^L_{Ln}) of **Ln-1** in the visible and NIR ranges have been determined. In the case of **Sm-1**, the values of Q^L_{Ln} in CH_3OH and CD_3OD solutions are exceptionally high, that is, 10.1(5) and 83(1) %. Values obtained for **Yb-1**, that is, 0.78(4) % in CH_3OH and 8.4(1)% in CD_3OD, are among the highest ones reported today for Yb^{3+} complexes formed with nondeuterated and nonhalogenated ligands.

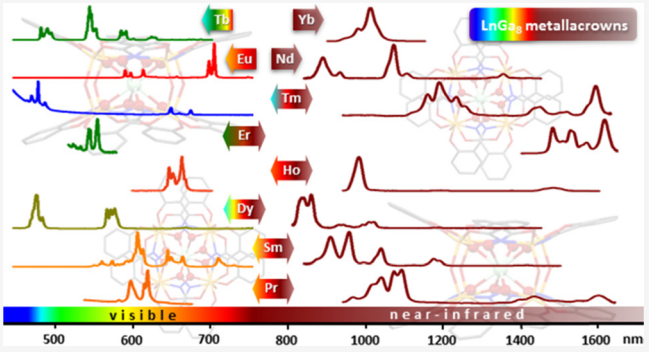

INTRODUCTION

Metallacrowns (MCs) constitute a class of supramolecular complexes that possess an $[M{-}N{-}O]_n$ repeating ring motif.[1,2] The M^{n+} ring cations are usually 3d transition metal ions (from vanadium(V) to zinc(II)), but MCs with the group 13 triels such as gallium(III)[3−6] or with 4d and 5d transition metal ions (e.g., palladium(II) and platinum(II))[7] have also been synthesized. Because of the diversity of structures and functional properties combined with the ease of synthesis via self-assembly under (typically) ambient temperature conditions, MCs have found a broad range of applications in different fields such as molecular recognition,[8−14] molecular magnetism,[15−23] and magnetorefrigeration,[24] as well as contrast agents for magnetic resonance imaging[25−27] or as luminescent probes for optical imaging.[28,29]

It has been shown that many MCs are able to bind a single or multiple trivalent lanthanide(III) ions (Ln^{3+}).[1] Ln^{3+} are widely studied for their unique optical properties derived from core-like valence 4f orbitals. Because 4f orbitals are present

Received: September 28, 2020
Revised: November 15, 2020
Published: December 2, 2020

https://dx.doi.org/10.1021/acs.jpca.0c08819
J. Phys. Chem. A 2020, 124, 10550−10564

within the 5s and 5p orbitals, they are largely shielded from crystal field and covalent bonding effects. Such an electronic structure results in Ln^{3+} displaying narrow and characteristic bands in their absorption and emission spectra from the corresponding f-f transitions, the positions of which are generally not significantly affected by the coordination environment or environmental conditions (e.g., pH, temperature, and biomolecules).[30] The characteristic emission of Ln^{3+} compounds that cover UV, visible, and near-infrared (NIR) ranges leads to their various applications in materials science[31] and biology:[32,33] from telecommunications,[34] secret tags,[35] lighting, display technologies,[36] and night-vision devices[37] to optical imaging and sensing.[38−41] Although Ln^{3+} luminescence is widely used, f-f transitions suffer from low molar absorptivities (<10 M^{-1} cm^{-1}) because of the Laporte- and spin- forbidden nature of most of such transitions. This forbiddance leads to experimentally useful long-lived excited state lifetimes of Ln^{3+}, but it implies that Ln^{3+} emission must be sensitized indirectly to obtain a significant emission intensity.[30] One of the strategies for Ln^{3+} sensitization is based on the 'antenna effect'[42] that is typically achieved by surrounding Ln^{3+} with organic chromophoric ligands. As a general scheme, the energy is absorbed by the ligand through singlet states ($S_0 \rightarrow S_n$) followed by internal conversion ($S_n \rightarrow S_1$) and intersystem crossing from excited singlet to excited triplet states ($S_1 \rightarrow T_1$), and then, in most of the cases, transfer from these excited states to the accepting electronic levels of Ln^{3+} ($S_1 \rightarrow Ln^{3+}$* and $T_1 \rightarrow Ln^{3+}$*).[30,43,44] Other processes such as metal to ligand charge transfer (MLCT) or inter- and intraligand charge transfer (ILCT) states may also play a role in the Ln^{3+} sensitization process.[45−50] Another challenge that has to be addressed when creating luminescent Ln^{3+}-based coordination compounds is the protection of Ln^{3+} against sources of nonradiative deactivations, which are most commonly because of overtones of O−H, N−H, and C−H vibrations.[51] The probability of this process is inversely proportional to the energy gap (ΔE) between the emitting level of the Ln^{3+} and the highest energy level of the ground multiplet. Thus, Eu^{3+} (12,300 cm^{-1}) and Tb^{3+} (14,800 cm^{-1}), having the largest ΔE (not considering UV-emitting Gd^{3+}), exhibit bright red and green emissions in their coordination compounds and are the most studied and exploited.[52−54] With respect to the NIR emission range, Yb^{3+} and Nd^{3+} complexes have been mainly considered.[38] Other luminescent Ln^{3+}, that is, Pr^{3+}, Sm^{3+}, Dy^{3+}, Ho^{3+}, Er^{3+}, and Tm^{3+}, usually exhibit less intense emission signals partially because of a smaller ΔE or because of the complex electronic structures with several emitting levels.[55] However, these Ln^{3+} possess an ability to emit in both the visible and NIR ranges.[47,50,56] Such dual-emission features of Ln^{3+} are less studied and exploited for coordination compounds[57−62] but can lead to, for example, the creation of sophisticated barcode modules[63−66] or novel optical imaging applications.[67,68]

We have recently reported several series of visible and NIR-emitting Ln^{3+}/Ga^{3+} MCs[3,5,6,69] and metallocryptates[70] assembled using salicylhydroxamic acid (H_3shi) as building blocks. We have demonstrated that Ga^{3+}/shi scaffolds possess a remarkable ability to sensitize the characteristic luminescence of bound visible and NIR-emitting Ln^{3+} including the dual-emitting Sm^{3+} and Dy^{3+}. However, quantitative photophysical properties (i.e., total (Q^{L}_{Ln}) and intrinsic (Q^{Ln}_{Ln}) quantum yields, observed (τ_{obs}) and radiative (τ_{rad}) lifetimes, and sensitization efficiencies (η_{sens})) have, despite the similarities between the Ga^{3+}/shi based scaffolds, been largely and in many cases unpredictably affected by the nature of the bridging ligands, counter-cations, crystal packing, and so forth.

Herein, we present the synthesis, characterization (including X-ray single crystal structural analysis), and detailed photophysical studies of a series of Ga^{3+}/Ln^{3+} MCs with the general composition $[LnGa_8(shi)_8(OH)_4]Na{\cdot}xCH_3OH{\cdot}yH_2O$ (**Ln-1**, Ln = Pr^{3+}−Yb^{3+}, excluding Pm^{3+}). The Y^{3+} analogue was also synthesized to facilitate characterization by ^1H NMR spectroscopy. Steady-state excitation and emission spectra were collected in the visible and/or the NIR ranges; Q^{L}_{Ln} and τ_{obs} were measured and analyzed for **Ln-1** in the solid state and, when possible, for solutions in CH_3OH and CD_3OD. The phosphorescence spectrum of **Gd-1** in the solid state was acquired to determine the energy position of the ligand triplet state. More detailed analyses of the photophysical properties, including the determination of τ_{rad}, Q^{Ln}_{Ln}, and η_{sens}, were performed for **Eu-1** and **Yb-1**.

The presented series of **Ln-1** MCs is remarkable relative to the Ga^{3+}/Ln^{3+} MCs that we have published previously.[3,5,6,69] In particular, Ln^{3+} in **Ln-1** adopt a pseudo-D_{4h} symmetry compared to C_4 or C_1 symmetries of our previously described MC systems. In addition, **Ln-1** possess a unique ability to sensitize the visible, NIR, or dual emissions of ten Ln^{3+} of different nature. The present structure is also the first MC in which efficient sensitization of red Eu^{3+} emission occurs. We should note that a Ga^{3+}/Dy^{3+} MC possessing a molecular geometry, which shares structural similarities to **Ln-1** but which is formed with another counter-cation (n-Bu_4N^+ vs Na^+), was obtained through a different synthetic route and was independently reported by the Rentschler group in a recent communication focused exclusively on single molecule magnet properties.[71] Luminescence properties were not described in that publication. It is important to note that we have previously evidenced that the nature of the counter-cation in the MC structure may significantly affect photophysical properties.[69]

METHODS

Excitation, Emission Spectra, Observed Lifetimes, and Quantum Yields. Luminescence data were collected for **Ln-1** samples in the solid state or on freshly prepared 50 μM solutions in CH_3OH and CD_3OD placed into 2.4 mm i.d. quartz capillaries or quartz Suprasil cells. Emission and excitation spectra were recorded on a Horiba-Jobin-Yvon Fluorolog 3 spectrofluorimeter equipped with either a visible photomultiplier tube (PMT) (220−800 nm, R928P; Hamamatsu), a NIR solid-state InGaAs detector cooled to 77 K (800−1600 nm, DSS-IGA020L; ElectroOptical Systems, Inc., USA), or a NIR PMT (950−1650 nm, H10330−75; Hamamatsu). All spectra were corrected for the instrumental functions. Luminescence lifetimes were determined under excitation at 355 nm provided by a Nd:YAG laser (YG 980; Quantel); the signals in the visible and the NIR ranges were detected with a R928 or H10330−75 PMT connected to an iHR320 monochromator (Horiba Scientific). The output signals from the detectors were fed into a 500 MHz bandpass digital oscilloscope (TDS 754C; Tektronix) and transferred to a PC for data processing with Origin 8 software. Luminescence lifetimes are averages of three or more independent measurements. Quantum yields were determined with a Fluorolog 3 spectrofluorimeter based on the absolute method using an integration sphere (GMP SA, Renens, Switzerland). Each

https://dx.doi.org/10.1021/acs.jpca.0c08819
J. Phys. Chem. A 2020, 124, 10550−10564

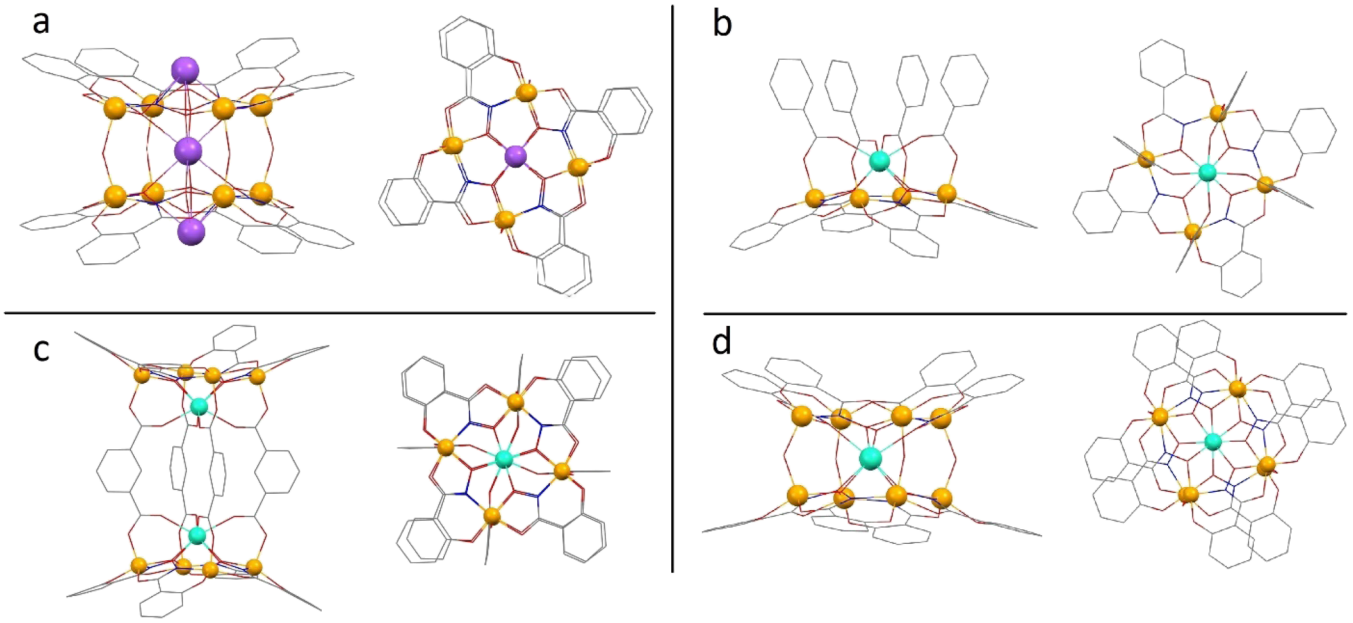

Figure 1. Side (left) and top-down (right) views of Ga^{3+}/shi MCs developed by our group. (a) $[Na_3Ga_8(shi)_8(OH)_4]$.[4] (b) $[DyGa_4(shi)_4(benzoate)_4]$.[5] (c) $[Dy_2Ga_8(shi)_8(isophthalate)_4]$.[3] (d) $[NdGa_8(shi)_8(OH)_4]$. Solvents of crystallization, nonintegral counter ions, and hydrogen atoms have been omitted for clarity. Color code: Ga, orange; Na, violet; Ln, teal; O, red; N, blue; C, grey.

sample was measured several times. The experimental error for the determination of quantum yields is estimated as ∼10%.

Phosphorescence Spectrum. The phosphorescence spectrum of **Gd-1** in the solid state at 77 K was acquired on a Horiba-Jobin-Yvon Fluorolog 3 spectrofluorimeter in time-resolved mode. See the Supporting Information for more details.

Diffuse Reflectance Spectra. For collection of diffuse reflectance spectra, **Ln-1** (5 wt %) were thoroughly ground with MgO. Measurements were performed on a Jasco V670 UV−visible spectrophotometer using a horizontal integration sphere accessory at room temperature.

Absorption Spectra. Absorption spectra (Figure S9) were collected on freshly prepared 50 μM solutions of **Ln-1** in methanol (Merck, Uvasol) placed in quartz cuvettes on a Jasco V670 UV−visible spectrophotometer in absorbance mode.

Synthesis and Characterization. All reagents and chemicals were purchased from commercial sources and used without further purification. All reactions were carried out aerobically under ambient conditions. Elemental analysis was performed by Atlantic Microlabs Inc. Electrospray ionization-mass spectrometry (ESI-MS) spectra were collected with an Agilent 6230 TOF HPLC-MS mass spectrometer in negative ion mode (−350 V) on samples dissolved in methanol or acetonitrile at a concentration of 2 mg/mL. Single crystals suitable for X-ray analysis were grown via slow evaporation from methanol/water solution at 295 K. See the Supporting Information for X-ray analysis details.

Salicylhydroxamic acid (H_3shi, 0.4 mmol), $Ln(NO_3)_3{\cdot}xH_2O$ (0.05 mmol, Ln^{3+} = Pr^{3+}, Nd^{3+}, Sm^{3+}, Eu^{3+}, Gd^{3+}, Tb^{3+}, Dy^{3+}, Ho^{3+}, Er^{3+}, Tm^{3+}, Yb^{3+}, and Y^{3+}), and $Ga(NO_3)_3{\cdot}xH_2O$ (0.4 mmol) were dissolved in 40 mL methanol. Concentrated (∼19.8 M) aqueous NaOH solution (1.4 mmol) was added, and the solution was stirred overnight. The solution was filtered, and the filtrate was left for slow evaporation, producing a crystalline compound within 2−3 weeks. The compound was collected via filtration and dried in air. See the Supporting Information for details.

NMR. One and two-dimensional ^{1}H NMR were performed on **Y-1** using a Varian VNMRS 500 MHz spectrometer equipped with a Varian 5 mm PFG OneNMR Probe. See the Supporting Information for details.

RESULTS

Synthesis and Crystal Structure of Ln-1. The reaction between $Ga(NO_3)_3{\cdot}xH_2O$, $Ln(NO_3)_3{\cdot}xH_2O$ (Ln = Y^{3+}, Pr^{3+}, Nd^{3+}, and Sm^{3+}−Yb^{3+}), and salicylhydroxamic acid (H_3shi) in a concentrated aqueous sodium hydroxide solution led to the formation of **Ln-1** with the general formula $[LnGa_8(shi)_8(OH)_4]Na{\cdot}xCH_3OH{\cdot}yH_2O$. Solids were collected as crystalline materials and characterized by ESI-MS, elemental analysis, and single crystal unit cell analysis.

X-ray quality crystals of **Nd-1** were grown from the slow evaporation of a methanol solution at ambient temperature. All compounds were found to have identical unit cells confirming the isostructural nature of the compounds (Table S2) and allowing a global description of molecular structures of this family of MCs.

The crystal structure of **Nd-1** is depicted in Figure 1d. It was solved in a monoclinic $P2_1/c$ group. Each molecule contains two $[12\text{-}MC_{Ga^{III}N(shi)}\text{-}4]$ units with composition that is identical to the MCs presented previously (Figure 1b,c).[3−5] Each of these MC units is slightly concave in nature and consists of four shi^{3-} ligands bridging four Ga^{3+} ions to form a neutral ring. The Nd^{3+} ion is located in the center of the two MC rings being bound to eight hydroximate oxygen ions (four from each ring) in a pseudosquare antiprismatic fashion. Each molecular unit contains a pseudo-D_{4h} symmetry about the Nd^{3+}. Each of the four MC Ga^{3+} ions is connected to a counterpart MC Ga^{3+} ion via a bidentate hydroxide [Ga-(μ_2OH)-Ga] bridge. The overall charge of the **Ln-1** MC is −1, balanced by a Na^+ cation.

https://dx.doi.org/10.1021/acs.jpca.0c08819
J. Phys. Chem. A 2020, 124, 10550−10564

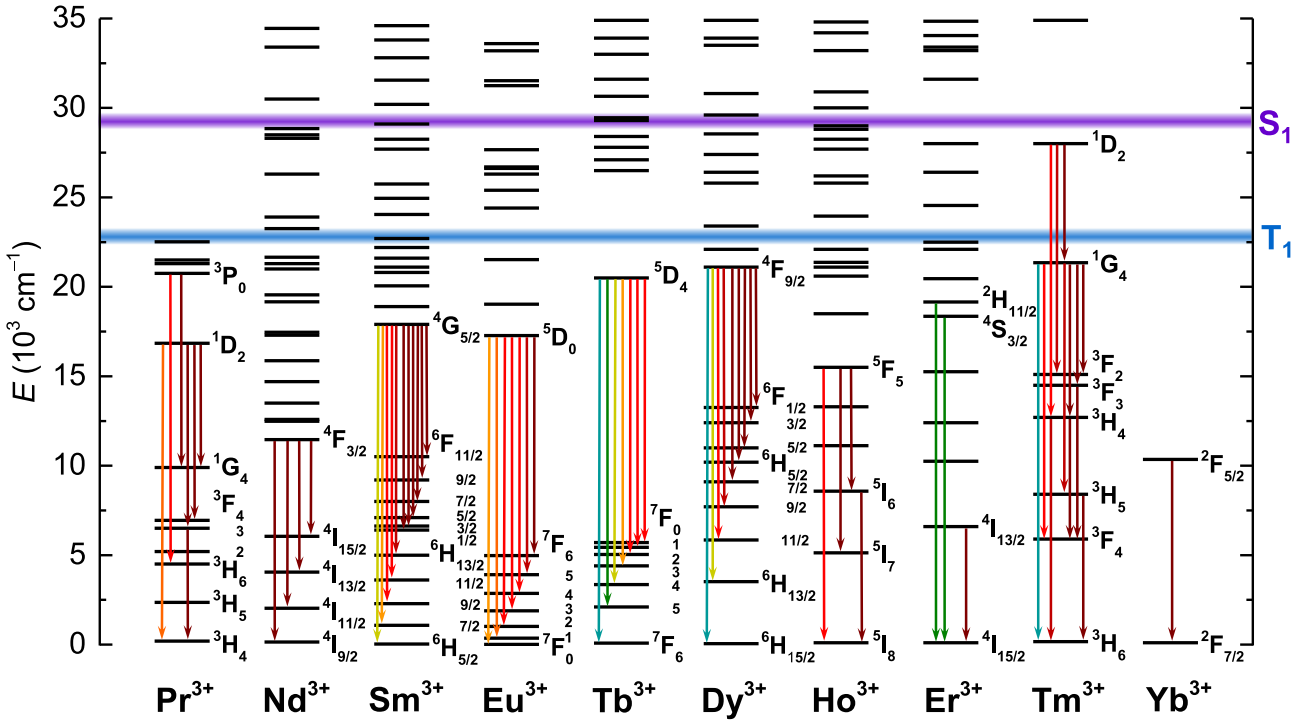

Figure 2. Lower energy part of the energy diagram of lanthanide(III) ions emitting in the visible and/or NIR range[79−81] and energy positions of the ligands singlet (S_1) and triplet (T_1) states of **Ln-1** MCs. Radiative transitions observed for **Ln-1** MCs are indicated with arrows.

There are two distinct complex structures present in the crystal of **Nd-1**. The first contains two *C* (clockwise) MC rings of the [-Ga-N-O-]$_4$ motif (when viewed with Nd^{3+} ions on the opposite side of the ring) binding a single Nd^{3+}, while the second complex contains two *A* (anticlockwise) MC rings of the [-Ga-O-N-]$_4$ motif binding a single Nd^{3+} (Figure S3). The nature of these complexes is consistent with an enantiomeric (nonsuperimposable mirror-image) relationship between the two isomers such that the above structural description is applicable to both of them. Their physical properties will generally be identical.

Charge neutrality is maintained, and the two isomers are bridged by two Na^+ such that discrete molecular dimers are present in the crystal (Figure S4). Each Na^+ is bound to a phenoxo oxygen and a hydroximate oxygen belonging to each of the two isomers. Each point of contact is additionally bonded to a Ga^{3+} ion in a [Ga-(μ_2O)-Na] organization. Two oxygens from solvent molecules complete the distorted six-coordinate geometry about the Na^+ ion. Different types of hydrogen bonds formed with solvents of crystallization (water and methanol) can be observed in the structure.

Behavior of Ln-1 in Solution. To assess the behavior of the complexes in solution, MS experiments were performed within a timeframe of 10−30 min after preparation of solutions of **Ln-1** in methanol and in acetonitrile. For each Ln^{3+} analogue in acetonitrile solution, a single large peak with isotopic distribution was identified (except for **Nd-1** and **Pr-1**, for which an additional feature was detected (Supporting Information)), which was consistent with the molecular formula of the monoanion $[LnGa_8(shi)_8(OH)_4]^-$ ($[M]^-$). This result suggests that the crystalline materials of **Ln-1** are isolated as $Na[LnGa_8(shi)_8(OH)_4]$.

For most Ln^{3+} analogues analyzed by MS in methanol solution, the base species $[M]^-$ were also identified; however, spectra were consistent with the presence of four additional species, that is, $[M + 14]^-$, $[M + 28]^-$, $[M + 42]^-$, and $[M + 56]^-$. These can be assigned to a sequential replacement of the bridging hydroxide ions (OH^-) with methoxide ions (CH_3O^-) as in the formula: $[LnGa_8(shi)_8(OH)_{4-n}(CH_3O)_n]^-$. This observation is in agreement with the exchange of CH_3O^- for OH^- from the gallium(III) ring metals across the entire series of Ln^{3+} MCs. The short timeline between the solution preparation (maximum 30 min) and the MS experiment suggests that CH_3O^-/OH^- exchange occurs rapidly in methanol solution. Over time, $[LnGa_8(shi)_8(CH_3O)_4]^-$ should become the dominant anion in solution given the prevalence of available CH_3O^- versus OH^- (in a 2 mM solution of **Ln-1** in methanol, the methanol concentration is 24.7 M) although differences in pKa between OH^- and CH_3O^- will also be relevant.[72]

To examine the solution stability further, we performed pulsed gradient spin echo diffusion ordered ^1H NMR spectroscopy (PGSE DOSY) on a diamagnetic Ln^{3+} analogue (**Y-1**) in CD_3OD.[73] The NMR signal response to increasing field gradient strength was fit quantitatively to determine experimental diffusion coefficients based on previously described procedures (Table S3).[74,75] In this experiment, it was found that all the identified MC protons migrate together within the time resolution of our experiment. In particular, no protons were found to migrate with a different diffusion coefficient, which would be an indication of decomposition of the MC. Calculations of the diffusion coefficient (*D*) based on the molecular weight and the Stokes−Einstein equation further support the stability of the MC dimer in solution (Figures S7, S8).[73] For the **Y-1** complex, a *D* value of $3.87{\cdot}10^{-10}$ m^2s^{-1} was calculated. For a hypothetical monomer of **Y-1**, we calculated $D = 4.73{\cdot}10^{-10}$ m^2s^{-1}. Finally, for a MC dimer with similar ethynylsalicylhydroximate ($eshi^{3-}$) ring ligands but a larger bridging ligand, that is, isophthalate, (iph^{2-}), and two Ln^{3+}, ($[Ln_2Ga_8(eshi)_8(iph)_4]$), $D = 3.17.10^{-10}$ m^2s^{-1} was reported.[76]

https://dx.doi.org/10.1021/acs.jpca.0c08819
J. Phys. Chem. A 2020, 124, 10550−10564

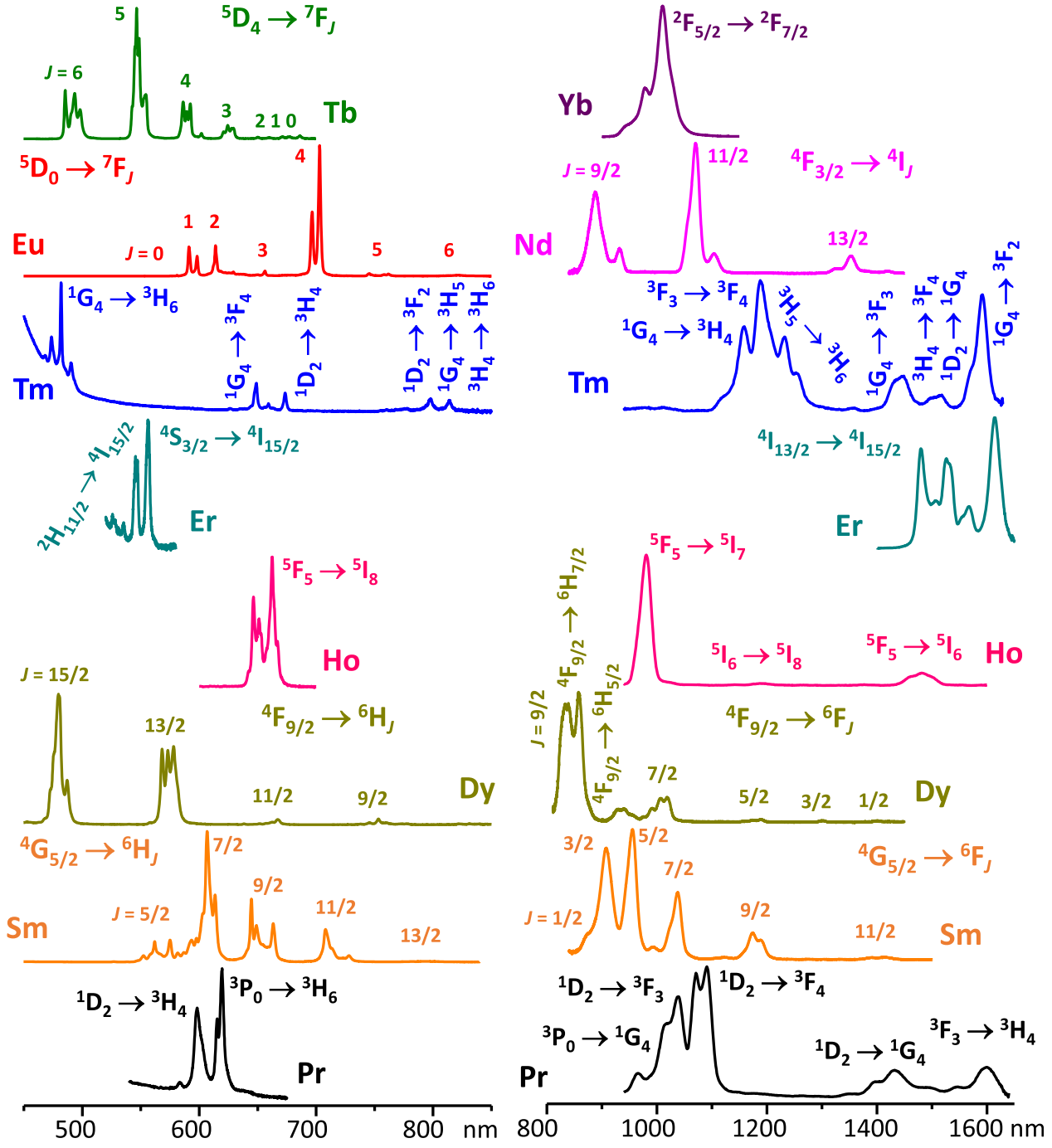

Figure 3. Highlights of the Ln^{3+}-centered emission signals of **Ln-1** MCs in the solid state under excitation at 340 nm at room temperature. Intensities of the emission spectra are normalized to the corresponding intensity maxima located in the range of 450−850 nm (left) or 800−1650 nm (right).

The experimental D value for **Y-1**, $4.23(8)\cdot10^{-10}$ m^2s^{-1}, is most similar to the calculated value for $Na[LnGa_8(shi)_8(OH)_4]$ and is an intermediate between the values calculated for the monomer and the larger dimer. This suggests that **Y-1** exists in solution as the $[YGa_8(shi)_8(OH)_{4-n}(CH_3O)_n]$ complex in agreement with the crystal structure and MS results.

Photophysical Properties. *Ligand-Centered Photophysical Properties.* Absorption spectra of **Ln-1** collected in methanol solution (Figure S9) are similar for all the MCs formed with the different Ln^{3+} and present broad bands in the UV region extending up to 350 nm that are attributed to $\pi \rightarrow \pi^*$ transitions. Apparent maxima of the lowest in energy absorption bands are located at 313−314 nm and have molar absorption coefficients of $\sim3.6\cdot10^4$ M^{-1} cm^{-1}. The energy of the ligand singlet state (S_1) determined from the edge of the absorption spectrum is located at 28690 cm^{-1} (348.5 nm). Diffuse reflectance spectra of **Ln-1**, similarly to absorption spectra, are dominated by broad-band $\pi \rightarrow \pi^*$ transitions in the UV range up to 370 nm (Figure S10). Sharp features attributed to f-f transitions have very weak contributions if diffuse reflectance spectra are presented as Kubelka−Munk function versus wavelength. All of the **Ln-1** complexes exhibit similar diffuse reflectance spectra except for **Eu-1** which has a small but distinct extension to the red side of the lowest energy

https://dx.doi.org/10.1021/acs.jpca.0c08819
J. Phys. Chem. A 2020, 124, 10550−10564

Table 1. Luminescence Lifetimes (τ_{obs}) and Ln^{3+}-Centered Quantum Yields Collected under Ligand Excitation (Q^{L}_{Ln}) for Ln-1[a]

Ln	state/ solvent	τ_{obs} (μs)[b]	level/ wavelength (nm)[c]	Q^{L}_{Ln} (%)[d] 450−800 nm	800−1650 nm
Pr	solid	0.101 (2)	$^1D_2$ / 1090	3.0 (2)·10^{-2}	4.91 (6)·10^{-3}
Nd	solid	0.91 (1)	$^4F_{3/2}$ / 1070		0.30 (2)
	CH_3OH	1.09 (3): 91 (2)% ;0.34 (3): 9 (2)%	″		0.167 (4)
	CD_3OD	5.9 (1): 89 (2)% ;2.0 (2): 10 (2)%	″		0.90 (2)
Sm	solid	151 (1)	$^4G_{5/2}$ / 611	10.4 (6)	0.193 (2)
	CH_3OH	83.4 (3)	″	10.1 (5)	7.98 (3)·10^{-2}
	CD_3OD	721 (3)	″	83 (1)	0.71 (2)
Eu	solid	1360 (10)	$^5D_0$ / 705	4.16 (6)	
	CH_3OH	1950 (1)	″	15.4 (1)	
	CD_3OD	2500 (10)	″	21 (1)	
Tb	solid	1040 (50): 87 (1)% ;390 (30): 13 (1)%	$^5D_4$ / 545	35 (2)	
	CH_3OH	1870 (10)	″	47.7 (2)	
	CD_3OD	1950 (10)	″	50.8 (9)	
Dy	solid	37.7 (8): 55 (1)% ;4.1 (1): 45 (1)%	$^4F_{9/2}$ /577	1.26 (7)	3.09 (9)·10^{-2}
	CH_3OH	24.8 (2): 87 (1)% ;2.69 (9): 13 (1)%	″	6.9 (3)	5.0 (2)·10^{-2}
	CD_3OD	41.5 (8): 92 (1)% ;4.54 (7): 8 (1)%	″	9.46 (6)	7.7 (4)·10^{-2}
Ho	solid	0.0385 (9)	$^5F_5$ / 980	2.20 (8)·10^{-2}	2.9 (3)·10^{-3}
Er	solid	1.93 (6)	$^4I_{13/2}$ / 1525	[e]	1.90 (4)·10^{-2}
Tm	solid	1.37 (1)	$^1G_4$ / 482	5.8 (2)·10^{-2}	4.7 (2)·10^{-5}
Yb	solid	27.4 (9)	$^2F_{5/2}$ / 1010		2.8 (1)
	CH_3OH	15.6 (2)	″		0.78 (4)
	CD_3OD	196 (1)	″		8.4 (1)

[a]For samples in the solid state or for 50 μM solutions in CH_3OH or CD_3OD, at room temperature, 2σ values between parentheses. Estimated experimental errors: τ_{obs}, ±2%; Q^{L}_{Ln} , ±10%. [b]Under excitation at 355 nm. If a biexponential decay was observed, population parameters $P_i = \frac{B_i\tau_i}{\sum_{i=1}^{n} B_i\tau_i}$ in % are given after the colon. [c]The main emitting level and the corresponding wavelength used to record luminescence decays. [d]Under excitation at 340 nm for the samples in the solid state and at 310 nm for solutions. [e]Too low to be determined.

band at ∼375 nm (Figure S10, right). This difference can likely be attributed to the lower reduction potential of Eu^{3+}/Eu^{2+} with respect to other Ln^{3+} and to the formation of a ligand-to-metal charge transfer (LMCT) state.

Gd^{3+} complexes serve as useful probes to assess the electronic structure of a ligand bound to Ln^{3+} because of the Gd^{3+} possessing an accepting energy level (32,000 cm^{-1})[77] that is too high to be populated by commonly used chromophoric organic ligands. Such complexes are therefore useful to assign ligand triplet (T_1) state energies as this state is not depopulated by Gd^{3+}. Moreover, its heavy-atom and paramagnetic effects facilitate intersystem crossing[78] and make phosphorescence emission arising from this T_1 state more probable and, in turn, more intense. The energy position of the T_1 level (22,620 cm^{-1} or 442 nm) was determined as the 0−0 transition from the phosphorescence spectrum of the **Gd-1** in the solid state recorded in time-resolved mode at 77 K under 340 nm pulsed excitation after a 200 μs delay between excitation and acquisition (Figure S11). The energy diagram reporting the energy positions measured for the S_1 and the T_1 states in **Gd-1** with respect to the electronic Ln^{3+} levels is presented in Figure 2.

Lanthanide-Centered Photophysical Properties. Excitation (Figure S12) and emission (Figure 3, Figure S13) spectra, Ln^{3+}-centered quantum yields under ligand excitation (Q^{L}_{Ln}), and observed luminescence lifetimes (τ_{obs}) (Table 1) were collected for all **Ln-1** (Ln = Pr^{3+}, Nd^{3+}, Sm^{3+}, Eu^{3+}, and Tb^{3+}−Yb^{3+}) in the solid state at room temperature. For the sake of comparison, Q^{L}_{Ln} values shown in Table 1 are reported separately for two ranges of emission wavelengths: 450−800 nm and 800−1650 nm. These are herein referred to as the visible and the NIR emission, respectively. In general, the emission efficiency of lanthanide(III) complexes can be described using the following equation:

$$Q^{L}_{Ln} = \eta_{sens} \cdot Q^{Ln}_{Ln} = \eta_{sens} \cdot \frac{\tau_{obs}}{\tau_{rad}} \quad (1)$$

where η_{sens} is the sensitization efficiency of the organic ligands that takes into account the energy migration processes occurring both within the ligands and from the ligand to the Ln^{3+} excited state; Q^{Ln}_{Ln} is the intrinsic quantum yield or quantum yield upon direct f-f excitation, it reflects the relative importance of radiative and nonradiative processes within Ln^{3+}; τ_{rad} is the radiative lifetime or the lifetime in the absence of nonradiative deactivation processes. Q^{Ln}_{Ln} is usually difficult to measure directly because of the very weak absorption of f-f transitions; however, it can be estimated as a ratio of τ_{rad} and the observed lifetimes (τ_{obs}).[43,82] The latter parameter is routinely accessed experimentally, but the determination of τ_{rad} is less straightforward.[83] Presently, we estimated τ_{rad} for **Yb-1** using its absorption spectrum (Supporting Information, Figure S19), and for **Eu-1** using its emission spectrum (vide infra).

To further establish the relationship between the structure and luminescence properties, a high-resolution emission spectrum was acquired for **Eu**-1 in the solid state (Figures S17, S18). To obtain information about the behavior of the studied MCs in solution and to assess the number of solvent molecules potentially coordinated to the Ln^{3+} (Supporting Information), a series of measurements was performed on solutions of selected **Ln-1** (Ln = Nd^{3+}, Sm^{3+}, Eu^{3+}, Tb^{3+}, Dy^{3+}, and Yb^{3+}) in CH_3OH and CD_3OD (Table 1, Figure 4, Figures S14 and S15). For the less luminescent **Ln-1** (Ln = Pr^{3+}, Ho^{3+},

https://dx.doi.org/10.1021/acs.jpca.0c08819
J. Phys. Chem. A 2020, 124, 10550−10564

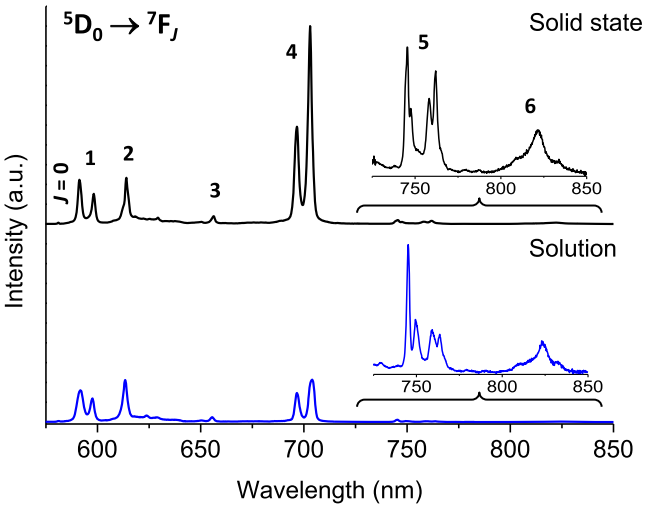

Figure 4. Comparison between emission spectra for **Eu-1** in the solid state (λ_{ex} = 340 nm) and in the 50 μM methanol solution (λ_{ex} = 310 nm) at room temperature (emission bandpass 1 nm and acquisition increment 0.2 nm). The spectra have been scaled so that the respective $^5D_0 \rightarrow {}^7F_1$ transitions have identical integrated areas.

Er^{3+}, and Tm^{3+}), excitation and emission spectra were only collected in CD_3OD (Figure S16). The assignment of the bands in the excitation and emission spectra was performed according to the existing literature.[79−81,84,85]

Excitation spectra collected for **Ln-1** in the solid state upon monitoring the main emission bands of the corresponding Ln^{3+} in the visible and/or the NIR ranges are dominated by broad ligand-centered bands in the UV up to 375 nm on the lower energy side or 425 nm in the case of **Eu-1** (Figure S12). The extension of the excitation band to the red for **Eu-1** is in line with the diffuse reflectance spectrum (Figure S10, right) and the formation of the LMCT state for this MC (vide supra) by describing the same electronic structure of the ligand−Eu^{3+} interaction. In addition to the broad bands present in the excitation spectra of all **Ln-1** (except **Yb-1**), sharper features that correspond to f-f transitions that are specific to the nature of the specific Ln^{3+} are observed. These bands have different relative intensities compared to the ligand-centered ones and vary between the particular Ln^{3+} of interest. For example, direct f-f excitation bands are almost inconsequential in the case of **Tb-1** while reaching 75% of the intensity of the ligand maximum signal for **Nd-1**. Excitation spectra of **Ln-1** measured in methanol solutions match the absorption spectra and present only broad bands in the UV up to 350 nm. The expanded excitation range for solid-state samples compared to those in solution can be explained by saturation effects.[86,87] All these observations reflect the ability of the MC scaffold in **Ln-1** to sensitize characteristic visible and NIR emissions of several Ln^{3+} of different nature through a common electronic structure.

Indeed, upon excitation into ligand-centered bands at 340 or 310 nm for samples in the solid state or in solution, respectively, **Ln-1** exhibit sharp emission bands in the visible and/or NIR ranges that are specific to the corresponding f-f transitions (Figure 3, Figures S13, S15, and S16).

Pr-1 in the solid state exhibits both visible and NIR emission bands arising mainly from $^1D_2$, but also from $^3P_0$ and $^3F_3$ excited state levels. Two visible emission bands are present in the range of 570−660 nm and are assigned to the $^1D_2 \rightarrow {}^3H_4$ and $^3P_0 \rightarrow {}^3H_6$ transitions with a Q^L_{Pr} value of $3.0 \cdot 10^{-2}$%. In the NIR domain, emission bands arise from the $^3P_0 \rightarrow {}^1G_4, {}^1D_2 \rightarrow {}^3F_3$, $^3F_4$, $^1G_4$, and $^3F_3 \rightarrow {}^3H_4$ electronic transitions and are observed in the range of 950−1650 nm. Q^L_{Pr} (NIR) was found to be $4.9 \cdot 10^{-3}$%, while the τ_{obs} value of the $^1D_2$ level is 101(2) ns. NIR emission of weaker intensity of **Pr-1** could be detected in CD_3OD solution (Figure S16).

Nd-1 in the solid state and CH_3OH and CD_3OD solutions shows NIR luminescence in the range of 850−1450 nm with three main bands at ∼885, 1065, and 1350 nm because of the $^4F_{3/2} \rightarrow {}^4I_J$ (J = 9/2−13/2) transitions. The general features of each of them remain similar for the sample in the solid state and in the solution. However, the relative intensity of the emission band corresponding to the $^4F_{3/2} \rightarrow {}^4I_{9/2}$ transition significantly increases for the latter. Luminescence decays are monoexponential for the solid-state sample and are biexponential in solution, with the 10% contribution of a short-lived component. τ_{obs} values are comparable for the solid-state sample and in solution in CH_3OH while Q^L_{Nd} is decreased from 0.3 to 0.17%. In CD_3OD solution, both τ_{obs} and Q^L_{Nd} are significantly increased reaching values of 5.9 μs and 0.9%, respectively.

Sm-1 emits in both visible and NIR, emission signals arising from the $^4G_{5/2}$ level, in the solid state and solutions. Multiple sharp emission bands in the visible range can be assigned to $^4G_{5/2} \rightarrow {}^3H_J$ (J = 5/2−13/2) transitions with $^4G_{5/2} \rightarrow {}^3H_{7/2}$ dominating the spectrum and being responsible for the pink-orange color of **Sm-1** emission. NIR emission is derived from $^4G_{5/2} \rightarrow {}^6F_J$ (J = 5/2−13/2) transitions. The crystal-field splitting of the emission bands is very similar for the **Sm-1** in the solid state and in solution but the relative intensities of the $^4G_{5/2} \rightarrow {}^3H_{9/2,\ 11/2}$, $^6F_{7/2,\ 9/2}$ transitions are smaller for the latter. A residual broad-band ligand-centered emission is observed at wavelengths <450 nm. Quantitative data are provided in Table S6. The values of Q^L_{Sm} (visible) are essentially the same (∼10%) for the sample in the solid state and in the CH_3OH solution, while τ_{obs} are 1.8-times shorter for the latter. Both parameters are drastically enhanced in CD_3OD solution reaching 83% and 721 μs. The values of Q^L_{Sm} in the NIR are lower and increase in the following order: CH_3OH < solid state < CD_3OD.

Eu-1 shows red luminescence with sharp emission bands assigned to $^5D_0 \rightarrow {}^7F_J$ (J = 0−6) transitions (Figure 4). The strictly forbidden $^5D_0 \rightarrow {}^7F_0$ transition results in an emission band possessing very low intensity. However, all the other transitions including the rarely observed $^5D_0 \rightarrow {}^7F_{5,6}$ can be clearly distinguished. In the solid state, the **Eu-1** emission spectrum is dominated by the $^5D_0 \rightarrow {}^7F_4$ transition that has 60.9% contribution to the total emission intensity (Table S4). The hypersensitive $^5D_0 \rightarrow {}^7F_2$ and magnetic dipole $^5D_0 \rightarrow {}^7F_1$ transitions have almost equal contribution with the ratio $I(^5D_0 \rightarrow {}^7F_2)/I(^5D_0 \rightarrow {}^7F_1)$ equal to 1.25. Such observations are consistent with a square antiprismatic environment around Eu^{3+} and a pseudo-D_{4h} symmetry (vide supra).[88] At room temperature, Q^L_{Eu} is equal to 4.2% while τ_{obs} is almost temperature independent (1.36 ms at 298 K vs 1.55 ms 10 K).

To gain more insight into the Eu^{3+} environment, a high-resolution emission spectrum of **Eu-1** in the solid state was recorded at 10 K (Figure S18). The narrow $^5D_0 \rightarrow {}^7F_0$ transition has a full-width at half-maximum (FWHM) of 10 cm^{-1} and a maximum at 17209 cm^{-1} (Figure S17). The observation of a single emission band for this transition reflects

https://dx.doi.org/10.1021/acs.jpca.0c08819
J. Phys. Chem. A 2020, 124, 10550−10564

the presence of only one type of emitting Eu^{3+} species in **Eu-1** and therefore of a unique environment around this metal ion. In addition, it is generally accepted that the energy of the $^5D_0 \rightarrow {}^7F_0$ transition ($\tilde{\nu}$) and, in particular, its shift from the energy determined for Eu^{3+} in the gas phase ($\tilde{\nu}_0$ = 17,374 cm^{-1}) depends on the nephelauxetic effect generated by the coordinating ligands. Several approaches have been suggested to estimate this effect,[89] but if considering the one by Frey and Horrocks:[90]

$$\tilde{\nu} = \tilde{\nu}_0 + C_{CN}\sum_{i=1}^{CN} n_i\delta_i \quad (2)$$

where δ_i is the nephelauxetic parameter for each coordinating ligand or group, n_i is the index of such groups, CN is the coordination number (CN = 8 for **Eu-1**), and C_{CN} is a coefficient that depends on CN (C_{CN} = 1.06 for CN = 8). If taking into account an approximation that $\tilde{\nu}$ increase by 1 cm^{-1} when the temperature rises by 24 K, $\tilde{\nu}$ equals to 17,221 cm^{-1} at 298 K. Therefore, δ_i = −18 for the shi^{3-} ligand's binding hydroximate oxygens, a value which is close to the effect induced by a charged carboxylate oxygen (δ_i = −18.2).[90] The $^5D_0 \rightarrow {}^7F_1$ transition contains two-fold degenerate and nondegenerate components that correspond to $^7F_1$ crystal-field sublevels located at 285.1, 335.3, and 506.2 cm^{-1} above the $^7F_0$ level. Such splitting reflects a pseudotetragonal symmetry around Eu^{3+} consistent with the square antiprism coordination environment.

The crystal-field splitting of $^5D_0 \rightarrow {}^7F_J$ (J = 0−6) transitions in the emission spectrum of **Eu-1** in methanol solution is very similar to those observed in the solid state (Figure 4). However, the contribution of the $^5D_0 \rightarrow {}^7F_4$ transition to the total emission intensity is decreased to 34.1% (vs 60.9% in the solid state). On the other hand, the ratio $I(^5D_0 \rightarrow {}^7F_2)/I(^5D_0 \rightarrow {}^7F_1)$ remains comparable (1.18 vs 1.25) (Table S4). Compared to the solid-state sample, the values of τ_{obs} and Q^L_{Eu} increase by 1.4 and 3.7 times, respectively, for **Eu-1** in CH_3OH solution. In deuterated solvent, these parameters increase by 1.8 and 5.0 fold, respectively (Table 2).

Table 2. Photophysical Parameters Obtained for Eu-1 in the Solid State and in 50 μM solutions[a]

state/ solvent	τ_{obs} (ms)	τ_{rad} (ms)[b]	Q^{Eu}_{Eu} (%)	Q^L_{Eu} (%)	η_{sens} (%)
Solid state	1.36 (1)	2.78	49	4.16 (6)	8.5
CH_3OH	1.95 (1)	7.80	24	15.4 (5)	62
CD_3OD	2.50 (1)	7.87	32	21 (1)	66

[a]At room temperature, 2σ values between parentheses. Relative errors: τ_{obs}, ±2%; Q^L_{Eu},±10%; τ_{rad}, ±10%; Q^{Eu}_{Eu}, ±12%; and η_{sens}, ±22%. [b]Calculated using eq 3 according to ref 91; n(solid state) = 1.5; $n(CH_3OH)$ = 1.33; and $n(CD_3OD)$ = 1.326.

To obtain more information about the parameters that affect the **Eu-1** emission intensity, τ_{rad} and the corresponding Q^{Eu}_{Eu} and η_{sens} were estimated using eq 1 (Table 2). In the case of Eu^{3+}, the $^5D_0 \rightarrow {}^7F_1$ transition has a purely magnetic dipolar character and is insensitive to the Eu^{3+} coordination environment and, when J-mixing is considered to be small, the integrated intensity of the $^5D_0 \rightarrow {}^7F_1$ transition (I_{MD}) can be used to calibrate the total integrated emission intensity arising from $^5D_0 \rightarrow {}^7F_J$ (J = 0−6) transitions (I_{tot}) and to determine τ_{rad} via the equation:[82,91]

$$\frac{1}{\tau_{rad}} = A_{MD,0}\cdot n^3\left(\frac{I_{tot}}{I_{MD}}\right) \quad (3)$$

where $A_{MD,0}$ is the spontaneous emission probability of the $^5D_0 \rightarrow {}^7F_1$ transition being equal to 14.65 s^{-1} and n is the refractive index. τ_{rad} is 2.8-fold longer for **Eu-1** in solution compared to those recorded in the solid state, leading to a 1.5−2 times decrease of the intrinsic quantum yields. On the other hand, the 7.3 fold increased sensitization efficiency of the ligands in solutions results in an overall increase of Q^L_{Eu}.

Tb-1 in the solid state and in solution exhibits a bright green emission arising from $^5D_4 \rightarrow {}^7F_J$ (J = 6−0) transitions with Q^L_{Tb} of 35−51%. The crystal field splitting of the $^5D_4 \rightarrow {}^7F_J$ bands is similar for **Tb-1** in the solid state and in solution (Figure S14). On the other hand, the relative integral intensity of the $^5D_4 \rightarrow {}^7F_6$ transition increases by 1.5 fold while for the other $^5D_4 \rightarrow {}^7F_J$ (J = 4−0) transitions a diminution by 1.4−3 fold is observed (Table S5). Experimental luminescence decays arising from the $^5D_4$ level in the solid state are best fitted with a biexponential function with the dominating contribution (87%) from the long component (1040 μs) and an average τ_{obs} value of 1010 μs. τ_{obs} measured at 10 K was found to be τ_1 = 1040(10) μs (P_1 = 96.4(4) %) and τ_2 = 272(5) μs (P_2 = 3.6(4) %) giving an average value of 1030 μs. The similarity of the average values of τ_{obs} when going from 298 to 10 K reflects the absence or an insignificant role of temperature dependent nonradiative processes including Boltzmann dependent back energy transfer in **Tb-1**. Luminescence decays of **Tb-1** in solution are monoexponential, and the corresponding τ_{obs} values are ∼2.2 times longer than those recorded in the solid state.

Dy-1 in the solid state and in solution emits both visible and NIR light originating from the $^4F_{9/2}$ level.[85] In the visible regime, the emission spectrum is dominated by the $^4F_{9/2} \rightarrow {}^6H_{15/2}$ transition centered at 480 nm, while in the NIR region the emission is dominated by the bands associated with the $^4F_{9/2} \rightarrow {}^6H_{9/2,\,7/2}$ transitions in the range of 800−880 nm. A residual broad-band ligand-centered emission <450 nm is observed (Figure S14, Table S6). The values of Q^L_{Dy} (visible) of **Dy-1** in CH_3OH and CD_3OD are 5.5 and 7.5 times higher than those in the solid state. Dy^{3+}-centered emission in the NIR is also enhanced in solution compared to the solid state but to a lesser extent, by a 1.6−2.5 fold. Luminescence decay curves recorded at 298 K upon monitoring the emission from the $^4F_{9/2}$ level are biexponential with an almost equal contribution from the short and the long components and the average value of 35 μs. At 10 K, the latter value is 3.5 times longer (123 μs) with respect to τ_1 = 125(1) μs (P_1 = 92.7(6)%) and τ_2 = 35(1) μs (P_2 = 7.3(6)%). Such behavior can be explained by the existence of the temperature-dependent nonradiative energy transfer processes such as the back transfer from the Dy^{3+} $^4F_{9/2}$ level (21,100 cm^{-1})[81] to the closely located triplet state of the ligands (22,620 cm^{-1}). In contrast to the behavior of **Tb-1**, **Dy-1** luminescence decays in solutions remain biexponential, although the contribution of the longer component is increased to 87−92% versus 55% for the solid state. The average τ_{obs} values are similar for the solid-state sample and the solution in CH_3OH (19.1 and 21.1 μs), but they increase to 37.9 μs for the CD_3OD solution.

Ho-1 in the solid state exhibits both visible and NIR emissions. The visible emission in the range of 635−680 nm is attributed to the $^5F_5 \rightarrow {}^5I_8$ transition and has a Q^L_{Ho} (visible) of

https://dx.doi.org/10.1021/acs.jpca.0c08819
J. Phys. Chem. A 2020, 124, 10550−10564

2.20(8)·10^{-2}%. The NIR emission signal is dominated by the $^5F_5 \rightarrow {}^5I_7$ transition at 980 nm with smaller contributions from the $^5F_5 \rightarrow {}^5I_6$ band at 1480 nm and a faint participation of the $^5I_6 \rightarrow {}^5I_8$ transition at 1190 nm. The observed luminescence lifetime of the $^5F_5$ level is 38.5(9) ns.

Er-1 in the solid state shows multiple emission bands located in the range of 1450−1650 nm and is assigned to the $^4I_{13/2} \rightarrow {}^4I_{15/2}$ transition. The luminescence decay of the $^4I_{13/2}$ level is monoexponential with a τ_{obs} value of 1.93(6) μs. Q^L_{Er} (NIR) is equal to 1.90(4)·10^{-2}%. In addition to the NIR emission, faint Er^{3+} transitions in the visible range between 520 and 565 nm because $^2H_{11/2} \rightarrow {}^4I_{15/2}$ and $^4S_{3/2} \rightarrow {}^4I_{15/2}$ transitions were detected; however, quantitative parameters related to these bands could not be determined.

Tm-1 possesses faint visible and NIR emissions with multiple bands arising from the $^1G_4$, $^1D_2$, $^3H_4$, and $^3F_3$ excited levels.[84] In the visible range, the $^1G_4 \rightarrow {}^3H_6$ transition with a maximum at 480 nm overlaps with the broad ligand-centered emission (Figure S13). Other bands are observed in the range of 620−840 nm. The total Q^L_{Tm} (visible) is equal to 5.8(2)·10^{-2}%, and the τ_{obs} of the $^1G_4$ level is 1.37(1) μs. Moreover, Tm^{3+} f-f specific electronic transitions with maxima at 1188, 1448, and 1592 nm could be detected in the range of 1100−1650 nm with Q^L_{Tm} (NIR) of 4.7(2) 10^{-5}%.

Yb-1 in the solid state and solutions displays NIR emission in the range of 920−1100 nm with a maximum at 1010 nm arising from the $^2F_{5/2} \rightarrow {}^2F_{7/2}$ transition. The values of τ_{obs} and Q^L_{Yb} decrease by 1.8 and 3.6 times, respectively, when comparing **Yb-1** in the solid state and in CH_3OH solution. In deuterated methanol, both values are significantly enhanced, reaching 196 μs and 8.4%. To obtain additional information about the different parameters that impact the global **Yb-1** emission efficiency, τ_{rad} was estimated from the absorption spectrum measured in the range of the $^2F_{5/2} \leftarrow {}^2F_{7/2}$ transition (Figure S19) using the modified Einstein's equation (Supporting Information).[91] The data are provided in Table 3 together with the values reported previously for other Yb^{3+}/Ga^{3+} MCs for comparison.

DISCUSSION

Synthesis and Characterization. **Ln-1** is the direct Ln^{3+}-centered analogue of the $[Na_3Ga_8(shi)_8(OH)_4]$ structure published previously by our group (Figure 1a).[4] It is also a major evolution of the Ga^{3+}/Ln^{3+} luminescent MCs created by us initially with the monomeric $[LnGa_4(shi)_4(benzoate)_4]$ (Figure 1b),[5] and then with the $[Ln_2Ga_8(shi)_8(isophthalate)_4]$ (Figure 1c)[3] series. The $[LnGa_8(shi)_8(OH)_4]$ MC (Figure 1d) possesses a pseudo-D_{4h} symmetry about the central Ln^{3+} as compared to the previously mentioned Ga^{3+}/Ln^{3+} MCs in which the Ln^{3+} is located on a pseudo-C_4 axis of symmetry.

The ESI-MS mass spectra of **Ln-1** measured in acetonitrile and methanol solutions revealed the exclusive presence of the MC species. The DOSY NMR data recorded on **Y-1** further support this observation (Supporting Information). Together, these results suggest that the **Ln-1** MCs are present as stable dimers in solution. However, in methanol solution, as indicated by MS experiments, a rapid OH^-/CH_3O^- exchange occurs which will eventually lead to CH_3O^- becoming the dominant bridging ion and $[LnGa_8(shi)_8(CH_3O)_4]$ becoming the main species.

Photophysical Properties. In the solid state, upon excitation into the ligand-centered bands at 340 nm, **Eu-1** and **Tb-1** exhibit bright red and green emission signals while **Yb-1** and **Nd-1** show their respective characteristic transitions in the NIR range (Figure 3). For **Pr-1**, **Sm-1**, **Dy-1**, **Ho-1**, **Er-1**, and **Tm-1**, dual-range emissions with bands located in the visible and NIR ranges were detected. It should be noted that such observation of dual emission for six Ln^{3+} using one type of molecular compound is very scarce.[47,50,56,62,92] Additionally, if the dual emission of Sm^{3+} and Dy^{3+} is more frequently observed and quantified,[3,5,6,46,47,57,60,65,67,68,85,93,94] studies that involve evaluation of such properties from Pr^{3+}, Ho^{3+}, Er^{3+}, and Tm^{3+} in coordination compounds are very rare.[58,59,61,64,95] However, unique bands arising from Ln^{3+} of different natures and spanning the whole visible and NIR ranges with various luminescence lifetimes and emission profiles are essential for multicolor and multiplex imaging[96,97] and could lead to the development of advanced materials such as sophisticated barcode modules[63−65] or other interesting optical imaging applications.[67,68]

It is generally accepted that the lowest energy triplet state of chromophoric ligands plays a predominant role in the sensitization of Ln^{3+} although singlet and charge transfer (CT) states may also be involved.[30,43] The energy position of the T_1 level determined from the phosphorescence spectrum of **Gd-1** was found at 22,620 cm^{-1}, a value similar to the ones observed for the previously reported series of MCs possessing a Ga^{3+}/shi scaffold, that is, $[LnGa_4(shi)_4(H_2shi)_2]$ (21,660 cm^{-1}),[6] $[LnGa_4(shi)_4(benzoate)_4]$ (22,170 cm^{-1}),[5] or $[Ln_2Ga_8(shi)_8(isophthalate)_4]$ (21,190 cm^{-1}).[3] The T_1 level in **Ln-1** is located slightly higher in energy than the emitting level of Dy^{3+}, ΔE ($T_1 - {}^4F_{9/2}$) = 1520 cm^{-1}, and a bit further from that of Tb^{3+}, ΔE ($T_1 - {}^5D_4$) = 2220 cm^{-1} (Figure 2). A relatively small difference in energy between the two levels increases the probability of thermally activated back $T_1 \leftarrow Ln^{3+}$* energy transfer. A clear influence of this process was confirmed for **Dy-1** with the 3.5 times lengthening of the average τ_{obs} value upon cooling from room temperature to 10 K. In the case of **Tb-1**, this effect is insignificant, and averaged τ_{obs} values are similar at both temperatures. Back energy transfer is probably responsible for the bi-exponential character of luminescence decays observed for **Tb-1** and **Dy-1** (Table 1). For **Tm-1** in the solid state, emission is originating from different electronic levels (Figures 2 and 3), that is, $^1D_2$ (28,000 cm^{-1}), $^1G_4$ (21,350 cm^{-1}), $^3H_4$ (12,700 cm^{-1}), and $^3H_5$ (8400 cm^{-1}). The T_1 level is positioned well above the $^3H_{4,5}$ levels but close to $^1G_4$ (ΔE ($T_1 - {}^1G_4$) = 1270 cm^{-1}) and is

Table 3. Photophysical Parameters Obtained for Yb-1 in Solution and Comparison with Other Yb^{III}/Ga^{III} MCs[a]

MC	solvent	τ_{obs} (μs)	τ_{rad} (μs)[b]	Q^{Yb}_{Yb} (%)	Q^L_{Yb} (%)	η_{sens} (%)
Yb-1	CH_3OH	15.6 (2)	814	1.9	0.78 (4)	41
	CD_3OD	196 (1)	819	24	8.4 (1)	35
$YbGa_4$ (1)[c]	CH_3OH	2.06 (4)	530	0.39	0.26 (1)	67
	CD_3OD	36.6 (1)	530	6.9	4.29 (1)	62
$YbGa_4$ (2)[d]	CH_3OH	1.72 (1)	590	0.29	0.123 (2)	42
	CD_3OD	27.4 (1)	590	4.6	2.55 (5)	55

[a]At room temperature, 2σ values between parentheses. Relative errors: τ_{obs}, ±2%; Q^L_{Yb}, ±10%; τ_{rad}, ±10%; Q^{Yb}_{Yb}, ±12%; and η_{sens}, ±22%. [b]See the Supporting Information for details; for CD_3OD solutions recalculated taking into account the refractive index $n(CD_3OD)$ = 1.326. [c]$[YbGa_4(shi)_4(benzoate)_4]$ from Ref.[5] [d]$[YbGa_4(shi)_4(H_2shi)_2]$ from Ref.[6]

https://dx.doi.org/10.1021/acs.jpca.0c08819
J. Phys. Chem. A 2020, 124, 10550−10564

significantly lower in energy than the $^1D_2$ level (ΔE (T_1−$^1D_2$) = −5380 cm^{-1}). The latter point suggests that Tm^{3+}-centered luminescence in **Tm-1** could be partially sensitized through the lowest singlet state of the ligands located at 28,690 cm^{-1}. For **Pr-1**, most of the emission bands originate from the $^1D_2$ (16,840 cm^{-1}) excited level; however, transitions from the $^3P_0$ (20,750 cm^{-1}) in the visible and the NIR ranges and from the $^3F_3$ (6500 cm^{-1}) in the NIR could also be detected (Figures 2 and 3). Emitting levels of other studied Ln^{3+} are located at least 3470 cm^{-1} below the energy of the T_1 level making it potentially well adapted for their sensitization (Figure 2).

In the case of **Eu-1** in the solid state, the slight broadening to the red of the diffuse reflectance spectrum is an indication of the presence of a LMCT. Such electronic states, depending on their energy position, can either quench or enhance Eu^{3+} luminescence.[45,49,98] Contrary to all of the Ga^{3+}/shi systems previously described by us where the formation of LMCT states either significantly[5] or fully[3,6,70] quench Eu^{3+} emission, **Eu-1** exhibited pronounced red emission (Figure 3). Therefore, this series of [$LnGa_8$(shi)$_8$(OH)$_4$] MCs is the first Ga^{3+}/shi MC scaffold that can efficiently sensitize Eu^{3+} luminescence. This luminescence originating mainly from $^5D_0 \rightarrow {}^7F_J$ (J = 0−6) transitions is not only interesting for numerous practical applications[52] but also from a theoretical point of view.[88] The nondegenerate character of the emitting $^5D_0$ level allows the easier interpretation of Eu^{3+} luminescence spectra. Therefore, the analysis of the relative intensities of $^5D_0 \rightarrow {}^7F_J$ (J = 0−6) transitions and their crystal-field splitting provide information about the point group symmetry and the coordination polyhedron around Eu^{3+}. Thus, interestingly, the emission spectrum of **Eu-1** in the solid state is dominated by the $^5D_0 \rightarrow {}^7F_4$ transition while the hypersensitive $^5D_0 \rightarrow {}^7F_2$ and magnetic dipole $^5D_0 \rightarrow {}^7F_1$ transitions have almost equal contributions (Figure 4, Table S4). These features reflect the square antiprismatic environment around the Eu^{3+} and the presence of a pseudo-D_{4h} symmetry,[88] in agreement with structural data. Further confirmation about the symmetry was obtained through the analysis of the fine splitting of the $^5D_0 \rightarrow {}^7F_1$ transition into two-fold degenerate and nondegenerate components in the high-resolution spectrum (Figure S17). Moreover, the presence of a single narrow $^5D_0 \rightarrow {}^7F_0$ transition (FWHM = 10 cm^{-1}) in the latter reflects the presence of only one type of emitting Eu^{3+} and therefore a unique and well-defined coordination environment around Eu^{3+} in **Eu-1**.

Dual emission of **Er-1** deserves special attention. Multiple emitting levels and small energy gaps facilitating nonradiative deactivation processes make the design of luminescent Er^{3+} compounds with organic ligands highly challenging.[30] Nevertheless, potential applications in telecommunications[34,99] of the Er^{3+} $^4I_{13/2} \rightarrow {}^4I_{15/2}$ transition with an emission wavelength at ∼1500 nm have initiated multiple attempts to create and enhance Er^{3+} emission in coordination compounds.[100−102] The observation of Er^{3+} transitions in the visible range is uncommon, and only a few examples could be found in the literature.[56,58,103,104] Nevertheless, we could unambiguously detect $^2H_{11/2} \rightarrow {}^4I_{15/2}$ and $^4S_{3/2} \rightarrow {}^4I_{15/2}$ transitions between 520 and 565 nm and as multiple bands in the range of 1450−1650 nm because of the $^4I_{13/2} \rightarrow {}^4I_{15/2}$ transition in the emission spectrum of **Er-1** in the solid state (Figure 2).

In CH_3OH and CD_3OD, solutions of **Ln-1** (Ln = Nd^{3+}, Sm^{3+}, Eu^{3+}, Tb^{3+}, Dy^{3+}, and Yb^{3+}) exhibit characteristic f-f transitions in the visible and/or NIR ranges upon excitation on chromophoric ligands at 310 nm. Compared to the corresponding emission spectra recorded in the solid state, a general trend was detected for all studied **Ln-1** in solution: the crystal-field splitting of f-f transitions remains the same while their relative intensities vary. The most significant change was observed for the **Eu-1** emission spectrum, which in the solid state is dominated by the $^5D_0 \rightarrow {}^7F_4$ transition. However, in solution, this band has an equal intensity to the hypersensitive $^5D_0 \rightarrow {}^7F_2$ transition (Figure 4, Table S4). Such variations are usually caused by changes in the coordination environment and symmetry around Ln^{3+}.[88] However, NMR studies and ESI-MS (vide supra) showed that the MC structure remains intact in solution while four OH^- bridges can be exchanged with CH_3O^-/CD_3O^-. Additionally, ESI-MS data show that, in solution, the solvation of the complex ion is likely to remove the coordination of two (1/2 equivalence) Na^+ ions bound at one side of the complex. This situation may lead to a more symmetrical structure in solution than in the solid state. Such behavior can affect the global electronic structure of the MC scaffold and may explain the changes of relative intensities of f-f transitions. Phenomenological equations[105] were used to estimate the number of solvent molecules coordinated to the Ln^{3+} based on the difference in τ_{obs} values recorded in both CH_3OH and CD_3OD solutions for **Eu-1**, **Tb-1**, and **Yb-1**. Results confirmed that this MC scaffold protects the coordinated Ln^{3+} ion well, and no solvent molecules are directly coordinated. It should be noted, however, that in the case of **Nd-1**, luminescence decays become bi-exponential in solution possibly because of the partial coordination of solvent molecules. Such observation could be explained by Nd^{3+} having a larger ionic radius, providing additional space for the access of quenching solvent molecules.

Quantitative photophysical parameters, in particular, the values of τ_{obs} and Q^L_{Ln} for **Ln-1** in the solid state, are comparable or superior (for **Eu-1** and **Sm-1**) to those reported previously for the [$LnGa_4$(shi)$_4$(benzoate)$_4$][5] or [Ln_2Ga_8(shi)$_8$(isophthalate)$_4$][3] MCs (Table S7). In protic solvents, the values of τ_{obs} and Q^L_{Ln} are usually lower than those measured in the solid state because of the higher probability of nonradiative deactivation through overtones of O−H vibrations.[30] Indeed, the values of Q^L_{Ln} measured for **Nd-1** and **Yb-1** and the NIR ($^4G_{5/2} \rightarrow {}^6F_J$) transitions of **Sm-1** are smaller in CH_3OH than in the solid state (Table 1). Nevertheless, the changes caused by the dissolution in a protic solvent are less significant than those reported previously for [$LnGa_4$(shi)$_4$(benzoate)$_4$].[5] Moreover, in the case of **Eu-1**, **Tb-1**, and **Dy-1** or visible ($^4G_{5/2} \rightarrow {}^3H_J$) transitions of **Sm-1**, the values of Q^L_{Ln} are, respectively, 3.7-, 1.4-, and 5.5-times higher or the same in CH_3OH solution than in the solid state. It should be noted that Q^L_{Sm} of **Sm-1** in CH_3OH solution (∼10%) is exceptionally high because this value usually does not exceed 2% for Sm^{3+} complexes in protic solvents,[106] while Q^L_{Yb} of **Yb-1** is three times larger with respect to the value recorded for [$YbGa_4$(shi)$_4$(benzoate)$_4$][5] (Table 3). In deuterated CD_3OD solutions of **Ln-1**, the values of τ_{obs} and Q^L_{Ln} are enhanced compared to those obtained in CH_3OH being in line with lower contribution of O−D vibrations to the nonradiative deactivation of Ln^{3+}.[105] This effect is the most sizable for **Sm-1** and **Yb-1**, the τ_{obs} and Q^L_{Ln} of which increase by 8−12 times reaching values of 721 μs/83% and 196 μs/8.4%, respectively (Table 1). These values are exceptional for Sm^{3+} coordination compounds[59,106−108] and are among the highest reported today for Yb^{3+} complexes formed with nondeuterated and nonhalogenated ligands.[51,69,109−111]

https://dx.doi.org/10.1021/acs.jpca.0c08819
J. Phys. Chem. A 2020, 124, 10550−10564

To quantify the parameters that impact the total quantum yield (Q^{L}_{Ln}) and to obtain a potential explanation for the photophysical properties of the studied series of Ln^{3+}/Ga^{3+} MCs, the values of τ_{rad} were determined for **Eu-1** (Table 2) and **Yb-1** (Table 3) using eq 3 and the modified Einstein's equation (Supporting Information), respectively. Furthermore, knowing τ_{rad}, τ_{obs}, and Q^{L}_{Ln} (Table 1), it is possible to estimate intrinsic quantum yields (Q^{Ln}_{Ln}) and sensitization efficiencies of the ligands, η_{sens}, according to eq 1.

It was found that τ_{rad} is equal to 2.78 ms for **Eu-1** in the solid state, a value that is close to the one reported, for example, for Eu^{3+} complexes formed with benzothiazole-substituted pyridine-2-carboxylate ligands (2.7−3.2 ms).[112] In CH_3OH or CD_3OD solutions, the value of τ_{rad} becomes 2.8-times longer (7.8 ms). Similar values were reported for aqueous solutions of Eu^{3+} helicates with pseudo-D_3 symmetry (6.2−6.9 ms).[113] Such changes of τ_{rad} are most probably induced by an exchange of four OH^- bridges with CH_3O^-/CD_3O^- in solution as suggested by MS data (vide supra). The lengthening of τ_{rad} leads to a decrease of Q^{Eu}_{Eu} by 1.5−2 times in solution compared to the value obtained in the solid state. Nevertheless, significantly improved η_{sens} (7.3−7.6 fold) in solutions of **Eu-1** results in a 3.7−5 times enhancement of Q^{L}_{Eu}.

In the case of **Yb-1**, the different photophysical parameters obtained in CH_3OH or CD_3OD solutions could be compared with the values reported for $[YbGa_4(shi)_4(benzoate)_4]$[5] and $[YbGa_4(shi)_4(H_2shi)_2]$[6] (Table 3). The values of τ_{rad} for **Yb-1** are 1.4−1.5 times longer than those for the other Yb^{3+}/Ga^{3+} MCs, probably, because of the higher level of symmetry around Yb^{3+} for the former one (pseudo-D_{4h} vs pseudo-C_4 or C_1). However, the values of Q^{Yb}_{Yb} are significantly (4.9−6.6 fold) higher for **Yb-1** than for the $[YbGa_4(shi)_4(benzoate)_4]$ and $[YbGa_4(shi)_4(H_2shi)_2]$ MCs because of the longer τ_{obs}. Notably, these two parameters observed for **Yb-1** are similar to the ones reported for Yb^{3+}/Zn^{2+} "encapsulated sandwich" MCs with quinaldichydroxamic acid, which similarly have a D_{4h}-type symmetry.[114] Finally, sensitization efficiencies for **Yb-1** are comparable or slightly lower than in $[YbGa_4(shi)_4(benzoate)_4]$ and $[YbGa_4(shi)_4(H_2shi)_2]$. Together with improved Q^{Yb}_{Yb} and τ_{obs} for **Yb-1**, we observed a more than 3.5−6.5 times enhancement of Q^{L}_{Yb} values in solution relative to the aforementioned Ln^{3+}/Ga^{3+} complexes.

Apart from the energy positions of the feeding levels (T_1, S_1, and CT) with respect to accepting Ln^{3+} levels, another aspect that is usually considered when designing luminescent Ln^{3+}-based coordination compounds is to avoid the presence of O−H, N−H, or C−H oscillators in close proximity to Ln^{3+} to prevent the quenching of their excited states. Therefore, the closest distances from Ln^{3+} to these oscillators were estimated for **Ln-1** (Figure S2). It was found that Ln···C−H is ∼7 Å, a value that is close to the one determined for Ln^{3+}/Zn^{2+} "encapsulated sandwich" MCs[114] and longer than that in $[LnGa_4(shi)_4(benzoate)_4]$[5] or $[Ln_2Ga_8(shi)_8(isophthalate)_4]$[3] (3.4−3.6 Å). However, the presence of O−H groups at ∼4 Å to Ln^{3+} in the crystal structure of **Ln-1** represents a source of nonradiative deactivations and is probably the reason for the slightly lower Q^{L}_{Ln} values for some of the **Ln-1** in the solid state compared to the $[LnGa_4(shi)_4(benzoate)_4]$[5] or $[Ln_2Ga_8(shi)_8(isophthalate)_4]$[3] MCs. On the other hand, in methanol solutions of **Ln-1**, while the molecular structure is preserved, four OH^- bridges are exchanged with CH_3O^-/CD_3O^- minimizing the sources of nonradiative deactivations that may explain comparable or higher Q^{L}_{Ln} with respect to those of the aforementioned Ln^{3+}/Ga^{3+}.

CONCLUSIONS

We have created, synthesized, and characterized a new series of $(Ga^{3+}_4)_2Ln^{3+}$ MCs (**Ln-1** where Ln = Y^{3+}, Pr^{3+}, Nd^{3+}, Sm^{3+}, Eu^{3+}, Gd^{3+}, Tb^{3+}, Dy^{3+}, Ho^{3+}, Er^{3+}, Tm^{3+}, and Er^{3+}) with the general composition $[LnGa_8(shi)_8(OH)_4]Na{\cdot}xCH_3OH{\cdot}yH_2O$ that possesses a pseudo-D_{4h} symmetry about the central Ln^{3+}. **Ln-1** in the solid state possess unique photophysical properties. In particular, this is the first example among different series of Ga^{3+}/Ln^{3+} MCs reported so far that exhibits an intense red Eu^{3+}-centered emission. Moreover, **Ln-1** contain the first MCs that demonstrate the exceptional ability to sensitize the emissions of six Ln^{3+} in a dual range of wavelengths (visible and NIR: Pr^{3+}, Sm^{3+}, Dy^{3+}, Ho^{3+}, Er^{3+}, and Tm^{3+}). In addition, **Yb-1** and **Nd-1** show characteristic emission in the NIR range while **Tb-1** exhibits bright green luminescence. Therefore, **Ln-1** is one of the few single-molecular complexes able to sensitize f-f transitions of ten out of fifteen trivalent Ln^{3+}, excluding La^{3+} ($4f^0$), Ce^{3+} (impeding 4f-5d transitions), Pm^{3+} (radioactive), Gd^{3+} (UV emission), and Lu^{3+} ($4f^{14}$). In addition, the structure of **Ln-1** remains intact in methanol solutions while four OH^- bridges are exchanged with CH_3O^-/CD_3O^- leading to comparable or improved photophysical properties as demonstrated for Ln = Nd^{3+}, Sm^{3+}, Eu^{3+}, Tb^{3+}, Dy^{3+}, and Yb^{3+}. The values of Q^{L}_{Ln} for **Sm-1** in the visible range are exceptionally high when recorded in both protic (CH_3OH, 10%) and deuterated solvents (CD_3OD, 83%) while those of **Yb-1** are among the highest reported today for Yb^{3+} complexes with nondeuterated and nonhalogenated ligands. These results demonstrate that $LnGa_8(shi)_8(OH)_4$ MCs are able to protect and sensitize Ln^{3+} emission throughout the visible and the NIR ranges opening new and broad perspectives for the exciting applications requiring such exceptional properties. This molecular system offers for the first time a large choice of lanthanide(III) emitters operating simultaneously in dual visible and NIR ranges, providing even more unique spectroscopic signatures.

ASSOCIATED CONTENT

Supporting Information

The Supporting Information is available free of charge at https://pubs.acs.org/doi/10.1021/acs.jpca.0c08819.

Crystallographic information file for **Nd-1** (CCDC 2008321) (CIF)

Experimental details, synthesis and characterization of **Ln-1** MCs, X-ray crystallographic parameters, ESI mass spectra, NMR studies, supplementary tables, and figures describing photophysical properties (PDF)

AUTHOR INFORMATION

Corresponding Authors

Svetlana V. Eliseeva − *Centre de Biophysique Moléculaire, Orleans Cedex 2, France;* orcid.org/0000-0002-1768-8513; Email: svetlana.eliseeva@cnrs-orleans.fr

Stéphane Petoud − *Centre de Biophysique Moléculaire, Orleans Cedex 2, France;* orcid.org/0000-0003-4659-4505; Email: stephane.petoud@inserm.fr

Vincent L. Pecoraro − *Department of Chemistry, Willard H. Dow Laboratories, University of Michigan, Ann Arbor,*

Michigan 48109, United States; orcid.org/0000-0002-1540-5735; Email: vlpec@umich.edu

Authors

Elvin V. Salerno − *Department of Chemistry, Willard H. Dow Laboratories, University of Michigan, Ann Arbor, Michigan 48109, United States;* orcid.org/0000-0003-3582-1012

Bernadette L. Schneider − *Department of Chemistry, Willard H. Dow Laboratories, University of Michigan, Ann Arbor, Michigan 48109, United States*

Jeff W. Kampf − *Department of Chemistry, Willard H. Dow Laboratories, University of Michigan, Ann Arbor, Michigan 48109, United States;* orcid.org/0000-0003-1314-8541

Complete contact information is available at: https://pubs.acs.org/10.1021/acs.jpca.0c08819

Author Contributions

‡E.V.S. and S.V.E contributed equally.

Notes

The authors declare no competing financial interest.

■ ACKNOWLEDGMENTS

This research was supported in part by the National Science Foundation (NSF) under the grant CHE-1664964 (V.L.P.). Acknowledgement is made for funding from NSF grant CHE-0840456 for X-ray instrumentation. E.V.S. thanks the Rackham Graduate School for international travel funding as well as NSF grant DGE-1256260. The work in France was supported by La Ligue Contre le Cancer and La Région Centre. S.P. acknowledges support from the Institut National de la Santé et de la Recherche Médicale (INSERM).

■ REFERENCES

(1) Lutter, J. C.; Zaleski, C. M.; Pecoraro, V. L. Metallacrowns: Supramolecular Constructs With Potential in Extended Solids, Solution-State Dynamics, Molecular Magnetism, and Imaging. *Adv. Inorg. Chem.* **2018**, *71*, 177−246.

(2) Mezei, G.; Zaleski, C. M.; Pecoraro, V. L. Structural and functional evolution of metallacrowns. *Chem. Rev.* **2007**, *107*, 4933−5003.

(3) Nguyen, T. N.; Chow, C. Y.; Eliseeva, S. V.; Trivedi, E. R.; Kampf, J. W.; Martinić, I.; Petoud, S.; Pecoraro, V. L. One-Step Assembly of Visible and Near-Infrared Emitting Metallacrown Dimers Using a Bifunctional Linker. *Chem. − Eur. J.* **2018**, *5*, 1031−1035.

(4) Lah, M. S.; Gibney, B. R.; Tierney, D. L.; Penner-Hahn, J. E.; Pecoraro, V. L. The fused metallacrown anion $Na_2\{[Na_{0.5}[Ga(salicylhydroximate)]_4]_2(\mu_2\text{-}OH)_4\}^-$ is an inorganic analog of a cryptate. *J. Am. Chem. Soc.* **1993**, *115*, 5857−5858.

(5) Chow, C. Y.; Eliseeva, S. V.; Trivedi, E. R.; Nguyen, T. N.; Kampf, J. W.; Petoud, S.; Pecoraro, V. L. Ga^{3+}/Ln^{3+} Metallacrowns: A Promising Family of Highly Luminescent Lanthanide Complexes That Covers Visible and Near-Infrared Domains. *J. Am. Chem. Soc.* **2016**, *138*, 5100−5109.

(6) Nguyen, T. N.; Eliseeva, S. V.; Chow, C. Y.; Kampf, J. W.; Petoud, S.; Pecoraro, V. L. Peculiarities of crystal structures and photophysical properties of Ga^{III}/Ln^{III} metallacrowns with a non-planar [12-MC-4] core. *Inorg. Chem. Front.* **2020**, *7*, 1553−1563.

(7) Teo, P.; Koh, L. L.; Hor, T. S. A. Na^+ and Ca^{2+} ion selective pyridylcarboxylate rings of Pd(II) and Pt(II). *Dalton Trans.* **2009**, *29*, 5637−5646.

(8) Cutland, A. D.; Malkani, R. G.; Kampf, J. W.; Pecoraro, V. L. Lanthanide 15-metallacrown-5 complexes form nitrate-selective chiral cavities. *Angew. Chem., Int. Ed.* **2000**, *39*, 2689−2692.

(9) Lim, C.-S.; Jankolovits, J.; Zhao, P.; Kampf, J. W.; Pecoraro, V. L. Gd(III) 15-metallacrown-5 recognition of chiral alpha-amino acid analogues. *Inorg. Chem.* **2011**, *50*, 4832−4841.

(10) Grant, J. T.; Jankolovits, J.; Pecoraro, V. L. Enhanced guest affinity and enantioselectivity through variation of the Gd^{3+} 15-metallacrown-5 side chain. *Inorg. Chem.* **2012**, *51*, 8034−8041.

(11) Sgarlata, C.; Giuffrida, A.; Trivedi, E. R.; Pecoraro, V. L.; Arena, G. Anion encapsulation drives the formation of dimeric Gd(III)[15-metallacrown-5](3+) complexes in aqueous solution. *Inorg. Chem.* **2017**, *56*, 4771−4774.

(12) Jankolovits, J.; Lim, C. S.; Mezei, G.; Kampf, J. W.; Pecoraro, V. L. Influencing the size and anion selectivity of dimeric Ln^{3+} 15-metallacrown-5 compartments through systematic variation of the host side chains and central metal. *Inorg. Chem.* **2012**, *51*, 4527−4538.

(13) Jankolovits, J.; Van-Noord, A. D. C.; Kampf, J. W.; Pecoraro, V. L. Selective anion encapsulation in solid-state Ln(III)[15-metallacrown-5]$^{3+}$ compartments through secondary sphere interactions. *Dalton Trans.* **2013**, *42*, 9803−9808.

(14) Piotrowski, H.; Polborn, K.; Hilt, G.; Severin, K. A self-assembled metallomacrocyclic ionophore with high affinity and selectivity for Li^+ and Na^+. *J. Am. Chem. Soc.* **2001**, *123*, 2699−2700.

(15) Chow, C. Y.; Bolvin, H.; Campbell, V. E.; Guillot, R.; Kampf, J. W.; Wernsdorfer, W.; Gendron, F.; Autschbach, J.; Pecoraro, V. L.; Mallah, T. Assessing the exchange coupling in binuclear lanthanide(III) complexes and the slow relaxation of the magnetization in the antiferromagnetically coupled Dy2 derivative. *Chem. Sci.* **2015**, *6*, 4148−4159.

(16) Boron, T. T., III; Lutter, J. C.; Daly, C. I.; Chow, C. Y.; Davis, A. H.; Nimthong-Roldán, A.; Zeller, M.; Kampf, J. W.; Zaleski, C. M.; Pecoraro, V. L. The Nature of the Bridging Anion Controls the Single-Molecule Magnetic Properties of DyX4M 12-Metallacrown-4 Complexes. *Inorg. Chem.* **2016**, *55*, 10597−10607.

(17) Zaleski, C. M.; Tricard, S.; Depperman, E. C.; Wernsdorfer, W.; Mallah, T.; Kirk, M. L.; Pecoraro, V. L. Single molecule magnet behavior of a pentanuclear mn-based metallacrown complex: solid state and solution magnetic studies. *Inorg. Chem.* **2011**, *50*, 11348−11352.

(18) Zaleski, C. M.; Depperman, E. C.; Kampf, J. W.; Kirk, M. L.; Pecoraro, V. L. Using Ln(III)[15-$MC_{Cu(II)(N)(S)\text{-}pheHA}$-5]$^{3+}$ complexes to construct chiral single-molecule magnets and chains of single-molecule magnets. *Inorg. Chem.* **2006**, *45*, 10022−10024.

(19) Zaleski, C. M.; Depperman, E. C.; Dendrinou-Samara, C.; Alexiou, M.; Kampf, J. W.; Kessissoglou, D. P.; Kirk, M. L.; Pecoraro, V. L. Metallacryptate Single-Molecule Magnets: Effect of Lower Molecular Symmetry on Blocking Temperature. *J. Am. Chem. Soc.* **2005**, *127*, 12862−12872.

(20) Zaleski, C. M.; Depperman, E. C.; Kampf, J. W.; Kirk, M. L.; Pecoraro, V. L. Synthesis, Structure, and Magnetic Properties of a Large Lanthanide−Transition-Metal Single-Molecule Magnet. *Angew. Chem., Int. Ed.* **2004**, *43*, 3912−3914.

(21) Boron, T. T., III; Kampf, J. W.; Pecoraro, V. L. A Mixed 3d−4f 14-Metallacrown-5 Complex That Displays Slow Magnetic Relaxation through Geometric Control of Magnetoanisotropy. *Inorg. Chem.* **2010**, *49*, 9104−9106.

(22) Happ, P.; Rentschler, E. Enforcement of a high-spin ground state for the first 3d heterometallic 12-metallacrown-4 complex. *Dalton Trans.* **2014**, *43*, 15308−15312.

(23) Happ, P.; Plenk, C.; Rentschler, E. 12-MC-4 metallacrowns as versatile tools for SMM research. *Coord. Chem. Rev.* **2015**, *289-290*, 238−260.

(24) Chow, C. Y.; Guillot, R.; Rivière, E.; Kampf, J. W.; Mallah, T.; Pecoraro, V. L. Synthesis and Magnetic Characterization of Fe(III)-Based 9-Metallacrown-3 Complexes Which Exhibit Magnetorefrigerant Properties. *Inorg. Chem.* **2016**, *55*, 10238−10247.

(25) Muravyeva, M. S.; Zabrodina, G. S.; Samsonov, M. A.; Kluev, E. A.; Khrapichev, A. A.; Katkova, M. A.; Mukhina, I. V. Water-soluble tetraaqua Ln(III) glycinehydroximate 15-metallacrown-5 complexes towards potential MRI contrast agents for ultra-high magnetic field. *Polyhedron* **2016**, *114*, 165−171.

(26) Katkova, M. A.; Zabrodina, G. S.; Muravyeva, M. S.; Shavyrin, A. S.; Baranov, E. V.; Khrapichev, A. A.; Ketkov, S. Y. Facile one-pot route toward water-soluble lanthanide-copper-glycinehydroximate 15-metallacrown-5 complexes. *Eur. J. Inorg. Chem.* **2015**, *2015*, 5202−5208.
(27) Parac-Vogt, T. N.; Pacco, A.; Nockemann, P.; Laurent, S.; Muller, R. N.; Wickleder, M.; Meyer, G.; Vander Elst, L.; Binnemans, K. Relaxometric study of copper [15] metallacrown-5 gadolinium complexes derived from alpha-aminohydroxamic acids. *Chem. − Eur. J.* **2006**, *12*, 204−210.
(28) Martinić, I.; Eliseeva, S. V.; Nguyen, T. N.; Foucher, F.; Gosset, D.; Westall, F.; Pecoraro, V. L.; Petoud, S. Near-Infrared Luminescent Metallacrowns for Combined in vitro Cell Fixation and Counter Staining. *Chem. Sci.* **2017**, *8*, 6042−6050.
(29) Martinić, I.; Eliseeva, S. V.; Nguyen, T. N.; Pecoraro, V. L.; Petoud, S. Near-Infrared Optical Imaging of Necrotic Cells by Photostable Lanthanide-Based Metallacrowns. *J. Am. Chem. Soc.* **2017**, *139*, 8388−8391.
(30) Bünzli, J.-C. G.; Eliseeva, S. V., Photophysics of Lanthanoid Coordination Compounds. In *Comprehensive Inorganic Chemistry II*, Yam, V. W.-W., Ed. Elsevier B.V.: Amsterdam, 2013; *8*, 339−398.
(31) Binnemans, K. Lanthanide-Based Luminescent Hybrid Materials. *Chem. Rev.* **2009**, *109*, 4283−4374.
(32) Bünzli, J.-C. G. Lanthanide Luminescence for Biomedical Analyses and Imaging. *Chem. Rev.* **2010**, *110*, 2729−2755.
(33) Eliseeva, S. V.; Bünzli, J.-C. G. Lanthanide luminescence for functional materials and bio-sciences. *Chem. Soc. Rev.* **2010**, *39*, 189−227.
(34) Ye, H. Q.; Li, Z.; Peng, Y.; Wang, C. C.; Li, T. Y.; Zheng, Y. X.; Sapelkin, A.; Adamopoulos, G.; Hernandez, I.; Wyatt, P. B.; Gillin, W. P. Organo-erbium systems for optical amplification at telecommunications wavelengths. *Nat. Mater.* **2014**, *13*, 382−386.
(35) Guillou, O.; Daiguebonne, C.; Calvez, G.; Bernot, K. A Long Journey in Lanthanide Chemistry: From Fundamental Crystallogenesis Studies to Commercial Anticounterfeiting Taggants. *Acc. Chem. Res.* **2016**, *49*, 844−856.
(36) SeethaLekshmi, S.; Ramya, A. R.; Reddy, M. L. P.; Varughese, S. Lanthanide complex-derived white-light emitting solids: A survey on design strategies. *J. Photochem. Photobiol. C: Photochem. Rev.* **2017**, *33*, 109−131.
(37) Wang, L.; Zhao, Z.; Wei, C.; Wei, H.; Liu, Z.; Bian, Z.; Huang, C. Review on the Electroluminescence Study of Lanthanide Complexes. *Adv. Opt. Mater.* **2019**, *7*, 1801256.
(38) Ning, Y.; Zhu, M.; Zhang, J.-L. Near-infrared (NIR) lanthanide molecular probes for bioimaging and biosensing. *Coord. Chem. Rev.* **2019**, *399*, 213028.
(39) Martinić, I.; Eliseeva, S. V.; Petoud, S. Near-infrared emitting probes for biological imaging: Organic fluorophores, quantum dots, fluorescent proteins, lanthanide(III) complexes and nanomaterials. *J. Lumin.* **2017**, *189*, 19−43.
(40) Mathieu, E.; Sipos, A.; Demeyere, E.; Phipps, D.; Sakaveli, D.; Borbas, K. E. Lanthanide-based tools for the investigation of cellular environments. *Chem. Commun.* **2018**, *54*, 10021−10035.
(41) Sy, M.; Nonat, A.; Hildebrandt, N.; Charbonniere, L. J. Lanthanide-based luminescence biolabelling. *Chem. Commun.* **2016**, *52*, 5080−5095.
(42) Weissman, S. I. Intramolecular Energy Transfer The Fluorescence of Complexes of Europium. *J. Chem. Phys.* **1942**, *10*, 214−217.
(43) Carneiro Neto, A. N.; Teotonio, E. E. S.; de Sá, G. F.; Brito, H. F.; Legendziewicz, J.; Carlos, L. D.; Felinto, M. C. F. C.; Gawryszewska, P.; Moura, R. T.; Longo, R. L.; et al., Modeling intramolecular energy transfer in lanthanide chelates: A critical review and recent advances. In *Handbook on the Physics and Chemistry of Rare Earths*, Bünzli, J.-C. G.; Pecharsky, V., Eds. 2019; *56*, 55−162.
(44) Junker, A. K. R.; Sørensen, T. J. Shining light on the excited state energy cascade in kinetically inert Ln(III) complexes of a coumarin-appended DO3A ligand. *Dalton Trans.* **2019**, *48*, 964−970.
(45) D'Aleo, A.; Pointillart, F.; Ouahab, L.; Andraud, C.; Maury, O. Charge transfer excited states sensitization of lanthanide emitting from the visible to the near-infra-red. *Coord. Chem. Rev.* **2012**, *256*, 1604−1620.
(46) Lo, W. S.; Zhang, J.; Wong, W. T.; Law, G. L. Highly luminescent Sm(III) complexes with intraligand charge-transfer sensitization and the effect of solvent polarity on their luminescent properties. *Inorg. Chem.* **2015**, *54*, 3725−3727.
(47) Pan, M.; Du, B. B.; Zhu, Y. X.; Yue, M. Q.; Wei, Z. W.; Su, C. Y. Highly Efficient Visible-to-NIR Luminescence of Lanthanide(III) Complexes with Zwitterionic Ligands Bearing Charge-Transfer Character: Beyond Triplet Sensitization. *Chem. − Eur. J.* **2016**, *22*, 2440−2451.
(48) Zhang, Z.; Zhou, Y.; Li, H.; Gao, T.; Yan, P. Visible light sensitized near-infrared luminescence of ytterbium via ILCT states in quadruple-stranded helicates. *Dalton Trans.* **2019**, *48*, 4026−4034.
(49) Nonat, A.; Esteban-Gómez, D.; Valencia, L.; Pérez-Lourido, P.; Barriada, J. L.; Charbonniere, L. J.; Platas-Iglesias, C. The role of ligand to metal charge-transfer states on the luminescence of europium complexes with 18-membered macrocyclic ligands. *Dalton Trans.* **2019**, *48*, 4035−4045.
(50) Liao, W.-M.; Li, C.-J.; Wu, X.; Zhang, J.-H.; Wang, Z.; Wang, H.-P.; Fan, Y.-N.; Pan, M.; Su, C.-Y. Homometallic Ln(III)-complexes from an ILCT ligand with sensitized vis-NIR emission, excitation-dependent PL color tuning and white-light emission. *J. Mater. Chem. C* **2018**, *6*, 3254−3259.
(51) Bünzli, J.-C. G. On the design of highly luminescent lanthanide complexes. *Coord. Chem. Rev.* **2015**, *293-294*, 19−47.
(52) Shuvaev, S.; Starck, M.; Parker, D. Responsive, Water-Soluble Europium(III) Luminescent Probes. *Chem. − Eur. J.* **2017**, *23*, 9974−9989.
(53) Hildebrandt, N.; Wegner, K. D.; Algar, W. R. Luminescent terbium complexes: Superior Förster resonance energy transfer donors for flexible and sensitive multiplexed biosensing. *Coord. Chem. Rev.* **2014**, *273-274*, 125−138.
(54) Petoud, S.; Cohen, S. M.; Bünzli, J.-C. G.; Raymond, K. N. Stable, high quantum yield lanthanide luminescence agents: multidentate 2-hydroxyisophatalamide complexes of Sm(III), Eu(III), Tb(III), Dy(III) in aqueous solution. *J. Am. Chem. Soc.* **2003**, *125*, 13324−13325.
(55) Liu, G. K., Electronic Energy Level Structure. In *Spectroscopic Properties of Rare Earths in Optical Materials*, Liu, G. K.; Jacquier, B., Eds. Springer Verlag: Berlin, 2005; *83*, 1−94.
(56) Sedykh, A. E.; Kurth, D. G.; Müller-Buschbaum, K. Two Series of Lanthanide Coordination Polymers and Complexes with 4′-Phenylterpyridine and their Luminescence Properties. *Eur. J. Inorg. Chem.* **2019**, *2019*, 4564−4571.
(57) Biju, S.; Gopakumar, N.; Bünzli, J.-C. G.; Scopelliti, R.; Kim, H. K.; Reddy, M. L. P. Brilliant Photoluminescence and Triboluminescence from Ternary Complexes of Dy^{III} and Tb^{III} with 3-Phenyl-4-Propanoyl-5-Isoxazolonate and a Bidentate Phosphine Oxide Coligand. *Inorg.Chem.* **2013**, *52*, 8750−8758.
(58) Golesorkhi, B.; Guénée, L.; Nozary, H.; Fürstenberg, A.; Suffren, Y.; Eliseeva, S. V.; Petoud, S.; Hauser, A.; Piguet, C. Thermodynamic Programming of Erbium(III) Coordination Complexes for Dual Visible/Near-Infrared Luminescence. *Chem. − Eur. J.* **2018**, *24*, 13158−13169.
(59) Ahmed, Z.; Iftikhar, K. Red, orange-red and near-infrared light emitting ternary lanthanide tris β-diketonate complexes with distorted C4v geometrical structures. *Dalton Trans.* **2019**, *48*, 4973−4986.
(60) Chen, L.; Zhang, H.; Pan, M.; Wei, Z. W.; Wang, H. P.; Fan, Y. N.; Su, C. Y. An Efficient Visible and Near-Infrared (NIR) Emitting Sm(III) Metal-Organic Framework (Sm-MOF) Sensitized by Excited-State Intramolecular Proton Transfer (ESIPT) Ligand. *Chem. − Asian J.* **2016**, *11*, 1765−1769.
(61) Dang, S.; Yu, J.; Yu, J.; Wang, X.; Sun, L.; Feng, J.; Fan, W.; Zhang, H. Novel Holmium (Ho) and Praseodymium (Pr) ternary complexes with fluorinated-ligand and 4,5-diazafluoren-9-one. *Mater. Lett.* **2011**, *65*, 1642−1644.

https://dx.doi.org/10.1021/acs.jpca.0c08819
J. Phys. Chem. A 2020, 124, 10550−10564

(62) Eliseeva, S. V.; Liasotkyi, V. S.; Golovach, I. P.; Doga, P. G.; Antonovich, V. P.; Petoud, S.; Meshkova, S. B. Exploring the ability of the nalidixate to sensitize visible and near-infrared emitting lanthanide(III) cations. *Methods Appl. Fluoresc.* **2017**, *5*, No. 014002.
(63) Wang, J.; Suffren, Y.; Daiguebonne, C.; Freslon, S.; Bernot, K.; Calvez, G.; Le Pollès, L.; Roiland, C.; Guillou, O. Multi-Emissive Lanthanide-Based Coordination Polymers for Potential Application as Luminescent Bar-Codes. *Inorg. Chem.* **2019**, *58*, 2659−2668.
(64) Du, B. B.; Zhu, Y. X.; Pan, M.; Yue, M. Q.; Hou, Y. J.; Wu, K.; Zhang, L. Y.; Chen, L.; Yin, S. Y.; Fan, Y. N.; Su, C. Y. Direct white-light and a dual-channel barcode module from Pr(III)-MOF crystals. *Chem. Commun.* **2015**, *51*, 12533−12536.
(65) Wang, S.; Xu, J.; Wang, J.; Wang, K.-Y.; Dang, S.; Song, S.; Liu, D.; Wang, C. Luminescence of samarium(III) bis-dithiocarbamate frameworks: codoped lanthanide emitters that cover visible and near-infrared domains. *J. Mater. Chem. C* **2017**, *5*, 6620−6628.
(66) White, K. A.; Chengelis, D. A.; Gogick, K. A.; Stehman, J.; Rosi, N. L.; Petoud, S. Near-Infrared Luminescent Lanthanide MOF Barcodes. *J. Am. Chem. Soc.* **2009**, *131*, 18069−18071.
(67) Foucault-Collet, A.; Shade, C. M.; Nazarenko, I.; Petoud, S.; Eliseeva, S. V. Polynuclear Sm(III) polyamidoamine-based dendrimer: a single probe for combined visible and near-infrared live-cell imaging. *Angew. Chem., Int. Ed.* **2014**, *53*, 2927−2930.
(68) Bui, A. T.; Grichine, A.; Brasselet, S.; Duperray, A.; Andraud, C.; Maury, O. Unexpected Efficiency of a Luminescent Samarium(III) Complex for Combined Visible and Near-Infrared Biphotonic Microscopy. *Chem. − Eur. J.* **2015**, *21*, 17757−17761.
(69) Lutter, J. C.; Eliseeva, S. V.; Collet, G.; Martinić, I.; Kampf, J. W.; Schneider, B. L.; Carichner, A.; Sobilo, J.; Lerondel, S.; Petoud, S.; Pecoraro, V. L. Iodinated metallacrowns: toward combined bimodal near-infrared and X-ray contrast imaging agents. *Chem. − Eur. J.* **2020**, *26*, 1274−1277.
(70) Lutter, J. C.; Eliseeva, S. V.; Kampf, J. W.; Petoud, S.; Pecoraro, V. L. A Unique Ln(III){[3.3.1]Ga(III) Metallacryptate} Series that Possesses Properties of Slow Magnetic Relaxation and Visible/Near-Infrared Luminescence. *Chem. − Eur. J.* **2018**, *24*, 10773−10783.
(71) Athanasopoulou, A. A.; Baldoví, J. J.; Carrella, L. M.; Rentschler, E. Field-induced slow magnetic relaxation in the first Dy(III)-centered 12-metallacrown-4 double-decker. *Dalton Trans.* **2019**, *48*, 15381−15385.
(72) Gao, D. Acidities of Water and Methanol in Aqueous Solution and DMSO. *J. Chem. Educ.* **2009**, *86*, 864−868.
(73) Cohen, Y.; Avram, L.; Frish, L. Diffusion NMR spectroscopy in supramolecular and combinatorial chemistry: an old parameter - new insights. *Angew. Chem., Int. Ed.* **2005**, *44*, 520−554.
(74) Zuccaccia, D.; Macchioni, A. An Accurate Methodology to Identify the Level of Aggregation in Solution by PGSE NMR Measurements: The Case of Half-Sandwich Diamino Ruthenium(II) Salts. *Organometallics* **2005**, *24*, 3476−3486.
(75) Cameron, K. S.; Fielding, L. NMR Diffusion Spectroscopy as a Measure of Host−Guest Complex Association Constants and as a Probe of Complex Size. *J. Org. Chem.* **2001**, *66*, 6891−6895.
(76) Lutter, J. C. *Refining Lanthanide Luminescence in Metallacrowns by Systematic Alteration of Hydroximate Ligand*. University of Michigan, 2018.
(77) Carnall, W. T.; Fields, P. R.; Rajnak, K. Electronic Energy Levels in the Trivalent Lanthanide Aquo Ions II. Gd(III). Absorption Spectra. *J. Chem. Phys.* **1968**, *49*, 4443−4446.
(78) Tobita, S.; Arakawa, M.; Tanaka, I. The paramagnetic metal effect on the ligand localized S1-to-T1 intersystem crossing in rare earth metal complexes with methyl salicylate. *J. Phys. Chem.* **1985**, *89*, 5649−5654.
(79) Carnall, W. T.; Fields, P. R.; Rajnak, K. Electronic Energy Levels in the Trivalent Lanthanide Aquo Ions IV. Eu(III). Absorption Spectra. *J. Chem. Phys.* **1968**, *49*, 4450−4455.
(80) Carnall, W. T.; Fields, P. R.; Rajnak, K. Electronic Energy Levels in the Trivalent Lanthanide Aquo Ions III Tb(III). *Absorption Spectra. J. Chem. Phys.* **1968**, *49*, 4447−4449.
(81) Carnall, W. T.; Fields, P. R.; Rajnak, K. Electronic Energy Levels in the Trivalent Lanthanide Aquo Ions I. Pr(III), Nd(III), Pm(III), Sm(III), Dy(III), Ho(III), Er(III) and Tm(III). *J. Chem. Phys.* **1968**, *49*, 4424−4442.
(82) Aebischer, A.; Gumy, F.; Bünzli, J.-C. G. Intrinsic quantum yields and radiative lifetimes of lanthanide tris(dipicolinates). *Phys. Chem. Chem. Phys.* **2009**, *11*, 1346−1353.
(83) Bünzli, J.-C. G.; Chauvin, A.-S.; Kim, H. K.; Deiters, E.; Eliseeva, S. V. Lanthanide Luminescence Efficiency in Eight- and Nine-coordinate Complexes: Role of the Radiative Lifetime. *Coord. Chem. Rev.* **2010**, *254*, 2623−2633.
(84) Blackburn, O. A.; Tropiano, M.; Sørensen, T. J.; Thom, J.; Beeby, A.; Bushby, L. M.; Parker, D.; Natrajan, L. S.; Faulkner, S. Luminescence and upconversion from thulium(III) species in solution. *Phys. Chem. Chem. Phys.* **2012**, *14*, 13378−13384.
(85) Kofod, N.; Arppe-Tabbara, R.; Sørensen, T. J. Electronic Energy Levels of Dysprosium(III) ions in Solution. Assigning the Emitting State and the Intraconfigurational 4f-4f Transitions in the Vis-NIR Region and Photophysical Characterization of Dy(III) in Water, Methanol, and Dimethyl Sulfoxide. *J. Phys. Chem. A* **2019**, *123*, 2734−2744.
(86) Wei, H.; Zhao, Z.; Wei, C.; Yu, G.; Liu, Z.; Zhang, B.; Bian, J.; Bian, Z.; Huang, C. Antiphotobleaching: A Type of Structurally Rigid Chromophore Ready for Constructing Highly Luminescent and Highly Photostable Europium Complexes. *Adv. Funct. Mater.* **2016**, *26*, 2085−2096.
(87) Ganapathi, M.; Eliseeva, S. V.; Brooks, N. R.; Soccol, D.; Fransaer, J.; Binnemans, K. Electrodeposition of luminescent composite metal coatings containing rare-earth phosphor particles. *J. Mater. Chem.* **2012**, *22*, 5514−5522.
(88) Binnemans, K. Interpretation of europium(III) spectra. *Coord. Chem. Rev.* **2015**, *295*, 1−45.
(89) Tanner, P. A.; Yeung, Y. Y.; Ning, L. What Factors Affect the 5D0 Energy of Eu3+? An Investigation of Nephelauxetic Effects. *J. Phys. Chem. A* **2013**, *117*, 2771−2781.
(90) Frey, S. T.; Horrocks, W. D., Jr. On Correlating the Frequency of the F-7(0)->D-5(0) Transition in Eu(3+) Complexes with the Sum of 'Nephelauxetic Parameters' for all of the Coordinating Atoms. *Inorg. Chim. Acta* **1995**, *229*, 383−390.
(91) Werts, M. H. V.; Jukes, R. T. F.; Verhoeven, J. W. The emission spectrum and the radiative lifetime of Eu^{3+} in luminescent lanthanide complexes. *Phys. Chem. Chem. Phys.* **2002**, *4*, 1542−1548.
(92) Wartenberg, N.; Raccurt, O.; Bourgeat-Lami, E.; Imbert, D.; Mazzanti, M. Multicolour Optical Coding from a Series of Luminescent Lanthanide Complexes with a Unique Antenna. *Chem. − Eur. J.* **2013**, *19*, 3477−3482.
(93) Sizov, V. S.; Komissar, D. A.; Metlina, D. A.; Aminev, D. F.; Ambrozevich, S. A.; Nefedov, S. E.; Varaksina, E. A.; Metlin, M. T.; Mislavskii, V. V.; Taydakov, I. V. Effect of ancillary ligands on visible and NIR luminescence of Sm(3+)beta-diketonate complexes. *Spectroc. Acta A* **2020**, *225*, 117503.
(94) Doffek, C.; Wahsner, J.; Kreidt, E.; Seitz, M. Breakdown of the energy gap law in molecular lanthanoid luminescence: the smallest energy gap is not universally relevant for nonradiative deactivation. *Inorg. Chem.* **2014**, *53*, 3263−3265.
(95) Wahsner, J.; Seitz, M. Perdeuterated 2,2′-bipyridine-6,6′-dicarboxylate: an extremely efficient sensitizer for thulium luminescence in solution. *Inorg. Chem.* **2013**, *52*, 13301−13303.
(96) Yakovliev, A.; Ziniuk, R.; Wang, D.; Xue, B.; Vretik, L. O.; Nikolaeva, O. A.; Tan, M.; Chen, G.; Slominskii, Y. L.; Qu, J.; Ohulchanskyy, T. Y. Hyperspectral Multiplexed Biological Imaging of Nanoprobes Emitting in the Short-Wave Infrared Region. *Nanoscale Res. Lett.* **2019**, *14*, 243.
(97) Li, H.; Wang, X.; Huang, D.; Chen, G. Recent advances of lanthanide-doped upconversion nanoparticles for biological applications. *Nanotechnology* **2020**, *31*, No. 072001.
(98) Faustino, W. M.; Malta, O. L.; Teotonio, E. E. S.; Brito, H. F.; Simas, A. M.; De Sá, G. F. Photoluminescence of Europium(III)

https://dx.doi.org/10.1021/acs.jpca.0c08819
J. Phys. Chem. A 2020, 124, 10550−10564

Dithiocarbamate Complexes: Electronic Structure, Charge Transfer and Energy Transfer. *J. Phys. Chem. A* **2006**, *110*, 2510−2516.
(99) Bünzli, J.-C. G.; Eliseeva, S. V. Lanthanide NIR luminescence for telecommunications, bioanalyses, and solar energy conversion. *J. Rare Earths* **2010**, *28*, 824−842.
(100) Winkless, L.; Tan, R. H. C.; Zheng, Y.; Motevalli, M.; Wyatt, P. B.; Gillin, W. P. Quenching of Er(III) luminescence by ligand C-H vibrations: Implications for the use of erbium complexes in telecommunications. *Appl. Phys. Lett.* **2006**, *89*, 111115.
(101) Ye, H. Q.; Peng, Y.; Li, Z.; Wang, C. C.; Zheng, Y. X.; Motevalli, M.; Wyatt, P. B.; Gillin, W. P.; Hernández, I. Effect of Fluorination on the Radiative Properties of Er^{3+} Organic Complexes: An Opto-Structural Correlation Study. *J. Phys. Chem. C* **2013**, *117*, 23970−23975.
(102) Hernández, I.; Gillin, W. P., Organic Chromophores-Based Sensitization of NIR-Emitting Lanthanides: Toward Highly Efficient Halogenated Environments. In *Handbook on the Physics and Chemistry of Rare Earths*, Bünzli, J.-C. G.; Pecharsky, V. K., Eds. Elsevier: 2015; *47*, 1−100.
(103) Suffren, Y.; Golesorkhi, B.; Zare, D.; Guenee, L.; Nozary, H.; Eliseeva, S. V.; Petoud, S.; Hauser, A.; Piguet, C. Taming Lanthanide-Centered Upconversion at the Molecular Level. *Inorg. Chem.* **2016**, *55*, 9964−9972.
(104) Nonat, A.; Chan, C. F.; Liu, T.; Platas-Iglesias, C.; Liu, Z.; Wong, W. T.; Wong, W. K.; Wong, K. L.; Charbonniere, L. J. Room temperature molecular up conversion in solution. *Nat. Commun.* **2016**, *7*, 11978.
(105) Beeby, A.; Clarkson, I. M.; Dickins, R. S.; Faulkner, S.; Parker, D.; Royle, L.; de Sousa, A. S.; Williams, J. A. G.; Woods, M. Non-radiative deactivation of the excited states of europium, terbium and ytterbium complexes by proximate energy-matched OH, NH and CH oscillators: an improved luminescence method for establishing solution hydration states. *J. Chem. Soc. Perkin Trans.* **1999**, *2*, 493−504.
(106) Melo, L. L. L. S.; Castro, G. P., Jr.; Gonçalves, S. M. C. Substantial Intensification of the Quantum Yield of Samarium(III) Complexes by Mixing Ligands: Microwave-Assisted Synthesis and Luminescence Properties. *Inorg. Chem.* **2019**, *58*, 3265−3270.
(107) Zhang, K.; Lin, M.-L.; Feng, C.-C.; Nie, P.-P.; Yang, Z.-R.; Chen, T.-T.; Zhang, L.-F.; Ma, S.; Shen, Y.-J.; Lu, Z.-Y. The efficient sensitization of Sm(III) ion by a macrocycle with the matched cavity and energy level. *Polyhedron* **2019**, *173*, 114133.
(108) Zhang, K.; Lu, Z. Y.; Feng, C. C.; Yang, Z. R.; Nie, P. P.; Chen, T. T.; Zhang, L. F.; Ma, S.; Shen, Y. J.; Lin, M. L. Series of Highly Luminescent Macrocyclic Sm(III) Complexes: Functional Group Modifications Together with Luminescence Performances in Solid-State, Solution, and Doped Poly(methylmethacrylate) Film. *ACS Omega* **2019**, *4*, 18334−18341.
(109) Kruck, C.; Nazari, P.; Dee, C.; Richards, B. S.; Turshatov, A.; Seitz, M. Efficient ytterbium near-infrared luminophore based on a nondeuterated ligand. *Inorg. Chem.* **2019**, *58*, 6959−6965.
(110) Ning, Y.; Tang, J.; Liu, Y.-W.; Jing, J.; Sun, Y.; Zhang, J.-L. Highly luminescent, biocompatible ytterbium(III) complexes as near-infrared fluorophores for living cell imaging. *Chem. Sci.* **2018**, *9*, 3742−3753.
(111) Hu, J.-Y.; Ning, Y.; Meng, Y.-S.; Zhang, J.; Wu, Z.-Y.; Gao, S.; Zhang, J.-L. Highly near-IR emissive ytterbium(III) complexes with unprecedented quantum yields. *Chem. Sci.* **2017**, *8*, 2702−2709.
(112) Shavaleev, N. M.; Scopelliti, R.; Gumy, F.; Bünzli, J.-C. G. Benzothiazole- and Benzoxazole-Substituted Pyridine-2-Carboxylates as Efficient Sensitizers of Europium Luminescence. *Inorg. Chem.* **2009**, *48*, 6178−6191.
(113) Bünzli, J.-C. G.; Chauvin, A.-S.; Vandevyver, C. D. B.; Bo, S.; Comby, S. Lanthanide Bimetallic Helicates for *in vitro* Imaging and Sensing. *Ann. N. Y. Acad. Sci.* **2008**, *1130*, 97−105.
(114) Trivedi, E. R.; Eliseeva, S. V.; Jankolovits, J.; Olmstead, M. M.; Petoud, S.; Pecoraro, V. L. Highly Emitting Near-Infrared Lanthanide "Encapsulated Sandwich" Metallacrown Complexes with Excitation Shifted Toward Lower Energy. *J. Am. Chem. Soc.* **2014**, *136*, 1526−1534.

https://dx.doi.org/10.1021/acs.jpca.0c08819
J. Phys. Chem. A 2020, 124, 10550−10564